Published in: Engineering Structures (2026), vol. 352, 122134
DOI: 10.1016/j.engstruct.2026.122134
Statut: Postprint (Author's version)

MECHANISTIC-DATA-DRIVEN MODELING OF MULTI-MATERIAL COMPOSITE COLUMNS: TOWARD INTELLIGENT LIGHTWEIGHT DESIGN

Shan Gao [a b], Jicheng Xu [a], Feng Fu [c], Zhenhua Huang [d], Jean Francois Demonceau [e], Jie Yang [b]

[a] *Shaanxi Key Laboratory of Safety and Durability of Concrete Structures, Xijing University, Xi'an, China*
[b] *School of Civil Engineering, Harbin Institute of Technology, Harbin, China*
[c] *Department of Engineering, School of Science & Technology, City, University of London, London, UK*
[d] *Department of Mechanical Engineering, University of North Texas, Denton, USA*
[e] *UEE Research Unit, University of Liège, Liège, Belgium*

Keywords: CFRP confinement; Composite columns; Lightweight design; Machine learning; Bearing capacity prediction

Abstract

This study examines the axial compressive performance of multi-material composite columns consisting of concrete-filled steel tubes with embedded CFRP-confined timber cores. A data-driven framework integrating theoretical model, finite element simulation and machine learning prediction is established to address the limited accuracy and scalability of conventional dual-material designs. An analytical bearing-capacity model is derived by accounting for steel confinement, CFRP hoop restraint, and timber orthotropy, of which results match FE results well with 5% deviations. Parametric investigations show that increasing steel yield strength and tube thickness would enhance the capacity of the composite columns, whereas CFRP confinement improves the post-crushing response and ductility of the timber core. The columns with circular cores exhibit better deformability than those with square ones. For axial bearing capacity prediction, a theory-residual-modified XGBoost model is proposed, in which theoretical estimates are corrected via SHAP-guided residual learning, achieving higher accuracy than single learners and ensemble baselines. A lightweight design tool is further developed for single/batch evaluation, automatic capacity-to-self-weight assessment, and interpretable prediction, enabling up to 22% self-weight reduction. The proposed methodology provides a validated and practical route for optimizing sustainable, lightweight multi-material composite columns.

1. Introduction

The evolution of modern construction toward taller and longer-span structures has rendered single-material systems inadequate for meeting the dual demands of combined load resistance and sustainable development. Studies [1] have shown that rationally combining two or more construction materials can significantly enhance structural strength, seismic performance, and life-cycle carbon

Published in: Engineering Structures (2026), vol. 352, 122134
DOI: 10.1016/j.engstruct.2026.122134
Statut: Postprint (Author's version)

efficiency. Current engineering practice primarily employs multi-material composite columns such as CFRP-confined concrete-filled steel tubes (CFSTs), FRP-wood hybrid columns, and steel-timber-concrete composites. However, material hybridization also introduces new challenges, including complex interfacial slip effects and incompatible failure modes [2]. Existing research has predominantly focused on bi-material systems, leaving the synergistic mechanisms of ternary and higher-order material combinations systematically underexplored, particularly when lightweight timber cores, steel-concrete confinement, and FRP hoop restraint coexist and interact under axial compression.

Regarding CFRP-confined concrete-filled steel tubular (CFST) columns, Wang et al. [3] experimentally investigated the axial compression behavior of circular CFRP-CFST stubs, demonstrating that CFRP wrapping significantly enhanced both the load-bearing capacity and ductility of the stubs. Wang et al. [4] conducted tests to analyze the effects of parameters such as the number of CFRP layers and the diameter-to-thickness ratio of the steel tube. They also proposed a bearing capacity calculation formula of CFRP-confined concrete-filled steel tubular columns based on Teng's models. In terms of FRP-wood interaction mechanisms, Shao et al. [5] confirmed that FRP confinement can enhance the performance of timber columns. Bukauskas et al. [6] further highlighted the significant influence of wood's anisotropic characteristics. However, this property has not been accurately represented in existing constitutive models [7], [8], [9], [10], [11], [12]. Liu et al. [13] explored a steel-timber composite structure and demonstrated the effectiveness of confinement, yet their theoretical model diverged from practical reality due to idealized assumptions regarding the connections.

The primary objective of multi-material coupling is to optimize structural performance by leveraging complementary material properties. For example, in steel tube-timber-concrete composite columns, partial substitution of concrete with timber significantly reduces structural self-weight, meeting lightweight design requirements. Li et al. [14] demonstrated numerically that steel tubes bear 60–70% of the axial load in square steel tube-timber-concrete columns. Wei et al. [15] found that a 10% increase in timber moisture content reduces the CFRP-timber interfacial bond strength by 30%, which is a critical parameter often overlooked in existing studies [7], [8], [9], [10], [11], [12], [13], [14], [15]. In numerical simulations, even when using the concrete damage plasticity model by Yuan et al. [16] and the constitutive model for timber proposed by Xia et al. [17], accurately simulating multi-material interfacial behavior remains challenging. Notably, even for steel-concrete multi-layer tubular systems, analytical characterization of interaction stress under axial compression has only been recently established, indicating that component interaction under axial load is nontrivial and becomes more complex when timber orthotropy and FRP confinement are involved [18]. Moreover, for non-circular sections, the confinement is intrinsically non-uniform. Recent mechanism-based studies on CFST columns have provided shape-affected reduction factors for equivalent confining stress. However these formulations are still developed for steel-concrete systems and have not been extended to four-material composite columns with CFRP-confined timber cores [19]. Meanwhile, conventional machine learning approaches are mostly limited to simple parametric analyses and lack an integrated cross-scale verification framework that accounts for material, environmental, and loading interactions [20], [21], [22], [23], [24].

In summary, existing research gaps manifest in two main aspects. When the four constituents, namely CFRP, timber, steel, and concrete, act in concert, each can contribute its functional advantages (e.g.,

Published in: Engineering Structures (2026), vol. 352, 122134
DOI: 10.1016/j.engstruct.2026.122134
Statut: Postprint (Author's version)

confinement, lightweighting, and load transfer), offering the potential to jointly optimize economic efficiency, environmental benefits, and mechanical performance. However, the resulting four-material interaction substantially increases system complexity, introducing stronger nonlinearities and multi-interface coupling behaviors that remain insufficiently understood. Most available studies concentrate on dual-material composite systems and lack systematic investigation of the synergistic mechanisms among CFRP-confined timber cores, steel tubes, and concrete, particularly the combined effects of timber lightweighting and steel-concrete confinement. Meanwhile, traditional numerical models are limited in describing multi-material coupling effects, where convergence can be highly sensitive to contact definitions, damage evolution, and stiffness degradation, making the coupled response difficult to robustly capture and consistently represent; meanwhile, machine learning applications remain largely confined to parametric fitting, with limited multiscale validation.

To address these gaps, this study develops a novel composite column that integrates CFRP-confined timber cores with concrete-filled steel tubes. Unlike previous CFRP-CFST studies [3], [4] that focused on dual-material systems, or FRP-timber research [5], [6] that neglected the combined effects of steel-concrete confinement, this study establishes a framework for CFRP-timber-steel-concrete composite columns. As illustrated in Fig. 1, to overcome the limitations of prior research [25], [26], this methodology integrates theoretical model, finite element simulation, and machine learning prediction, with experimental validation, thereby providing a comprehensive framework spanning from multi-physics modeling to data-driven optimization. While existing machine learning methods [20], [21], [22], [23], [24] are largely limited to parametric fitting and lack physical interpretability, the proposed TRM-XGBoost framework is built upon mechanics-based formulas.

Fig. 1. Comprehensive analysis flowchart for axial compressive bearing capacity of novel composite columns.

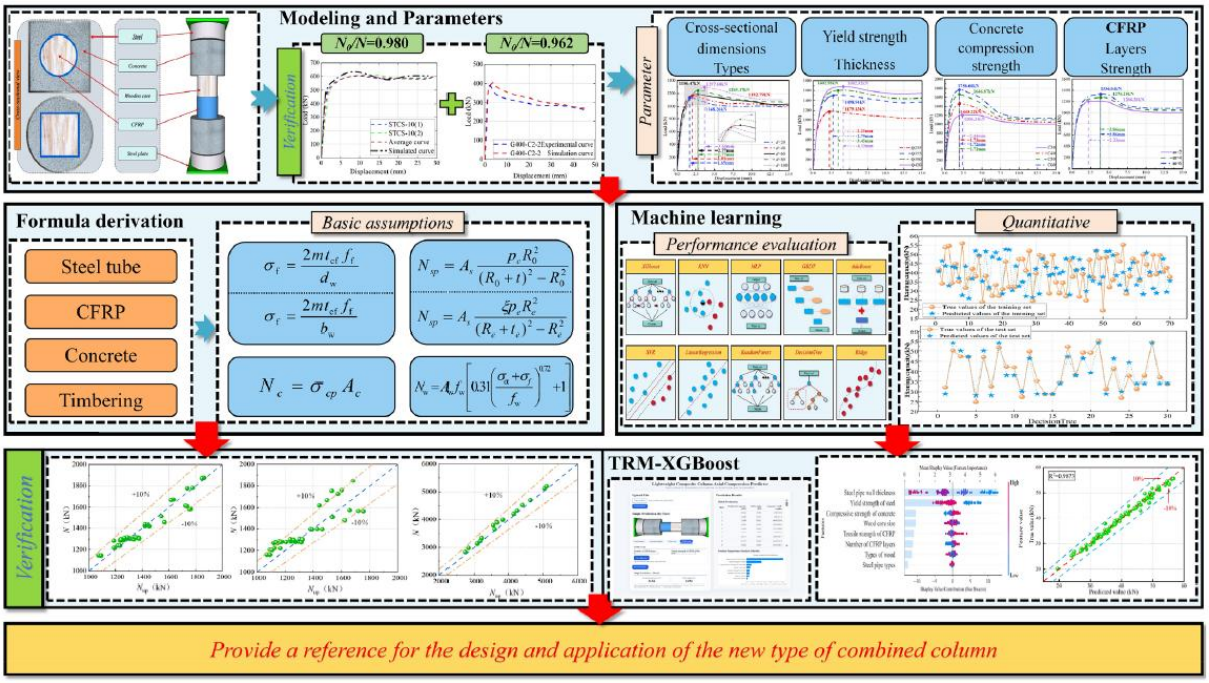

Published in: Engineering Structures (2026), vol. 352, 122134
DOI: 10.1016/j.engstruct.2026.122134
Statut: Postprint (Author's version)

2. Simulation methodology

2.1. COMPOSITE COLUMN DESIGN

Two types of concrete-filled steel tube composite columns (square (SC) and circular-section (CC)) were designed, together with their corresponding CFRP-reinforced components (Fig. 2).

Fig. 2. Structural configuration of concrete-filled steel columns with CFRP-confined timber cores.

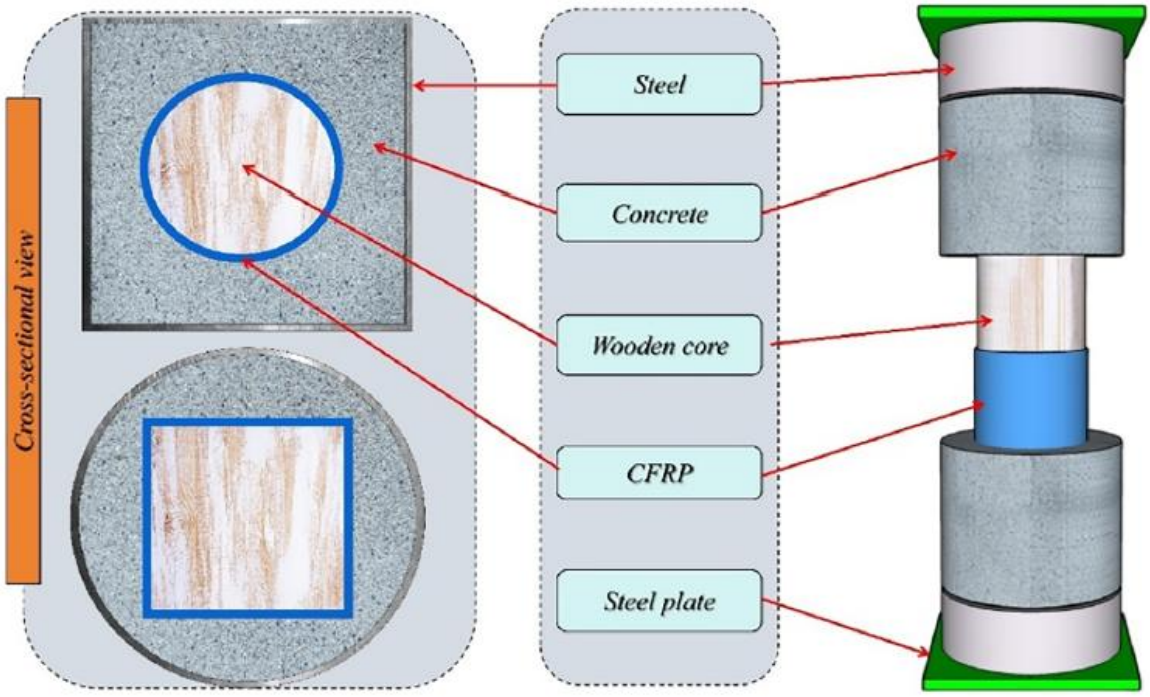

Axial compression tests revealed clear differences in mechanical performance: the square steel tube concrete column (SC, B = 150 mm, t = 4 mm, f_{cu} = 30 MPa) exhibited an ultimate bearing capacity of 1233 kN, while its CFRP-reinforced variants included a square timber core (SCS, b = 60 mm, A_w = 3600 mm², m = 2 layers, f_f = 3227.4 MPa, N = 1270 kN) and a circular timber core (SCC, d = 67.6 mm, A_w = 3590 mm², m = 2 layers, f_f = 3227.4 MPa, N = 1265 kN). By contrast, the circular steel tube concrete column (CC, D = 160 mm, t = 4 mm, f_{cu} = 30 MPa) showed an ultimate capacity of 1188 kN, with its CFRP-reinforced counterparts comprising a square timber core (CCS, b = 60 mm, A_w = 3600 mm², m = 2 layers, f_f = 3227.4 MPa, N = 1179 kN) and a circular timber core (CCC, d = 67.6 mm, A_w = 3590 mm², m = 2 layers, f_f = 3227.4 MPa, N = 1207 kN). All specimens were fabricated using larch wood.

2.2. FINITE ELEMENT MODELING

2.2.1. STEEL MATERIAL PROPERTIES

The constitutive relationship of the steel tube is the quadratic plastic flow model illustrated in Fig. 3 [27], involving five phases: the linear elastic stage (oa), elastoplastic stage (ab), yielding stage (bc), hardening stage (cd), and softening stage (de).

Published in: Engineering Structures (2026), vol. 352, 122134
DOI: 10.1016/j.engstruct.2026.122134
Statut: Postprint (Author's version)

$$\sigma = \begin{cases} E_s\varepsilon_s & (\varepsilon_s \le \varepsilon_p) \\ -A\varepsilon_s{}^2 + B\varepsilon_s + C & (\varepsilon_p < \varepsilon_s \le \varepsilon_{y1}) \\ f_y & (\varepsilon_{y1} < \varepsilon_s \le \varepsilon_{y2}) \\ \left(1 + 0.6(\varepsilon_s - \varepsilon_{y2})/(\varepsilon_u - \varepsilon_{y2})\right) f_y & (\varepsilon_{y2} < \varepsilon_s \le \varepsilon_u) \\ 1.6 f_y & (\varepsilon_s > \varepsilon_u) \end{cases} \quad (1)$$

Where A is 0.2 $f_y/(\varepsilon_{y1} - \varepsilon_{y2})^2$; B is $2A\varepsilon_{yl}$; C is $0.8f_y + A\varepsilon_p^2 - B\varepsilon_p$; f_p is $0.8f_y$; ε_e is $0.8f_y$ / E_s; ε_{e1} is $1.5\varepsilon_p$; ε_{y2} is 10 ε_{y1} ; ε_u is 100 ε_{y1} ; E_s is elastic modulus of steel (MPa); f_p is the proportional limit of steel(MPa); f_y is the yield strength of steel (MPa); f_u is the ultimate tensile strength of steel (MPa).

Fig. 3. Stress-strain relationship curve of steel.

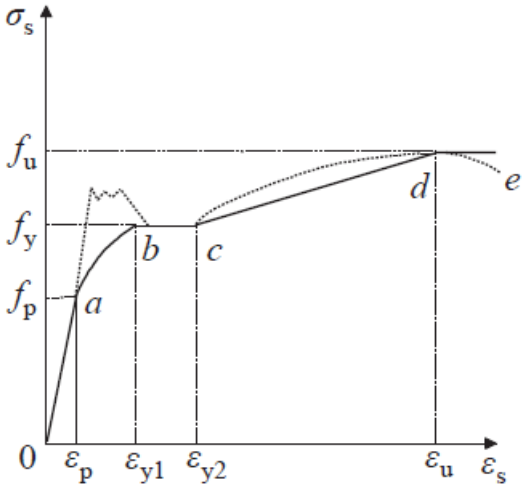

2.2.2. CONCRETE MATERIAL PROPERTIES

Tao [28] developed a compressive constitutive model for confined concrete based on concrete damage plasticity material model, as shown in Fig. 4.

$$\sigma = \begin{cases} f_c'\left(\dfrac{AX + BX^2}{1 + (A - 2X) + (B + 1)X^2}\right) (0 < \varepsilon \le \varepsilon_{c0}) \\ f_c'(\varepsilon_{c0} \le \varepsilon < \varepsilon_{cc}) \\ f_r + (f_c' - f_r)\exp\left[-\left(\dfrac{\varepsilon - \varepsilon_{cc}}{a}\right)^{\beta}\right] (\varepsilon \ge \varepsilon_{cc}) \end{cases} \quad (2)$$

Where X is ε / ε_{c0}; A is $E_c\varepsilon_{c0}/f_c'$; B is $(A-1)^2$ / 0.55 − 1; f_c' is $[0.76 + 0.2\log_{10}\left(\frac{f_{cu}}{19{,}6}\right)] f_{cu}$; ε_{c0} is $0.00076 + \sqrt{(0.626\, f_c' - 4.33) \times 10^{-7}}$.

Published in: Engineering Structures (2026), vol. 352, 122134
DOI: 10.1016/j.engstruct.2026.122134
Statut: Postprint (Author's version)

$$\frac{\varepsilon_{cc}}{\varepsilon_{c0}} = e^{K},\ K = \left(2.9224 - 0.00367 f_c'\right)\left(\frac{f_B}{f_c'}\right)^{0.3124 + 0.002 f_c'} \tag{3}$$

$$f_B = \begin{cases} \dfrac{\left(1 + 0.027 f_{y1}\right) e^{-0.02\frac{D_1}{t_1}}}{1 + 1.6 e^{-10}\left(f_c'\right)^{4.8}} \left(\text{circular} - \text{section}\right) \\ \dfrac{0.25\left(1 + 0.027 f_{y1}\right) e^{-\frac{0.02\sqrt{B^2 + D^2}}{t}}}{1 + 1.6 e^{-10}\left(f_c'\right)^{4.8}} \left(\text{square} - \text{section}\right) \end{cases} \tag{4}$$

$$f_r = \begin{cases} 0.7\left(1 - e^{-1.38\xi_c}\right) f_c' \left(\text{circular} - \text{section}\right) \\ 0.1 f_c' \left(\text{square} - \text{section}\right) \end{cases} \tag{5}$$

$$\alpha = \begin{cases} 0.04 - \dfrac{0.036}{1 + e^{6.08\xi_c - 3.49}} \left(\text{circular} - \text{section}\right) \\ 0.05 + 0.0075\xi_c \left(\text{square} - \text{section}\right) \end{cases} \tag{6}$$

Where ξ_c is $A_s f_y$ / $A_c f_c'$; E_c is $4700\sqrt{f_c'}$.

Fig. 4. Uniaxial compressive stress-strain curve of concrete.

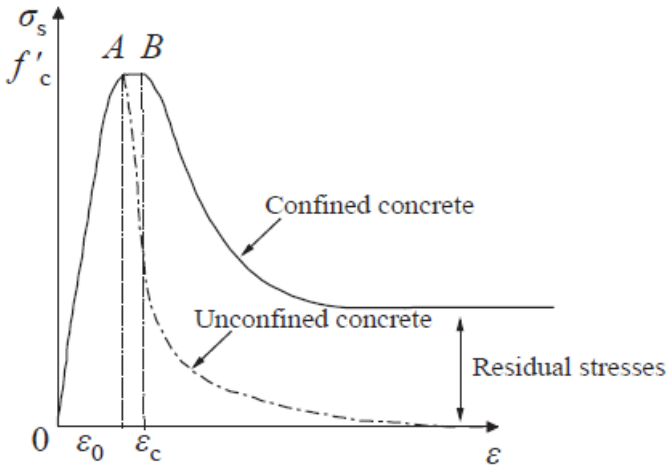

Concrete Damaged Plasticity (CDP)Model is selected to characterize the mechanical behavior of concrete in composite columns under axial compression. The default value of Eccentricity (e) of the flow potential is 0.1. Based on the investigation of Ref. [29], Viscosity coefficient μ is set to 0.0005. Biaxial-to-uniaxial compressive yield stress ratio f_{b0}/f_c' is determined using the formulation of Papanikolaou and Kappos [30], calculated as:

$$f_{b0}/f_c' = 1.5\left(f_c'\right)^{0.075} \tag{7}$$

K_c is the ratio of the second stress invariant on the tensile meridian to that on the compressive meridian. Uenaka et al. [31] investigated the influence of K_c on the *N*-ε curve. Building on the work of Yu T [32], the following expression is used:

Published in: Engineering Structures (2026), vol. 352, 122134
DOI: 10.1016/j.engstruct.2026.122134
Statut: Postprint (Author's version)

$$K_c = 5.5/(5+2(f_c')^{0.075}) \quad (8)$$

The parameter ψ characterizes the dilatancy of the concrete yield surface during the hardening stage, which is primarily governed by the combined effects of the confining stress state and accumulated plastic deformation in the core concrete. The following regression-based formula is used, proposed by Yu et al. [32]:

$$\psi = \begin{cases} 56.3(1-\xi) & \xi \le 0.5 \\ 6.672e^{7.4/(4.64+\xi)} & \xi > 0.5 \end{cases} \quad (9)$$

Tao [28] proposed a stress-strain relationship model for concrete under uniaxial tension:

$$G_f = (0.0469d_{max}^2 - 0.5d_{max} + 26)(f_c'/10)^{0.7} \quad (10)$$

where d_{max} denotes the maximum coarse aggregate size. A default of d_{max} = 20 mm is adopted.

2.2.3. WOOD PROPERTIES

To accurately describe the mechanical behavior of wood, its material properties must be defined separately in the longitudinal, radial, and tangential directions [33], [34], [35]. Based on the actual load-response characteristics of wood, an idealized elastic-plastic model was therefore adopted to simulate plastic deformation and softening capacity after yielding, as shown in Fig. 5.

$$\sigma_{cs} = \begin{cases} \varepsilon_{cs}E_{cs} (0 < \varepsilon_{cs} < \varepsilon_{c0}) \\ f_{ce} (\varepsilon_{c0} < \varepsilon_{cs} < \varepsilon_{cu}) \end{cases} \quad (11)$$

Fig. 5. Longitudinal compressive stress-strain curve of wood.

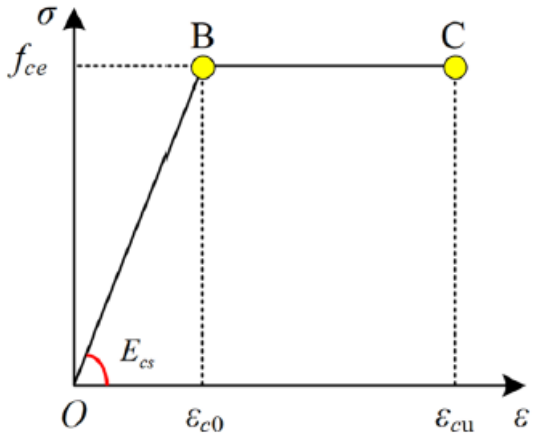

Where f_{ce} is the ultimate longitudinal compressive strength of wood (MPa); E_{cs} is the elastic modulus under longitudinal compression (MPa); ε_{c0} is a strain at the ultimate compressive strength (peak stress point); ε_{cu} is the ultimate longitudinal compressive strain (strain at failure).

(1) Wood elastic parameters

In ABAQUS, the elastic properties of orthotropic materials can be defined using either the Orthotropic (stiffness matrix) method or the Engineering Constants method. The Engineering Constants approach is adopted to define the nine elastic constants of wood, where E_1, E_2, and E_3 correspond to the

Published in: Engineering Structures (2026), vol. 352, 122134
DOI: 10.1016/j.engstruct.2026.122134
Statut: Postprint (Author's version)

longitudinal elastic modulus E_L, radial elastic modulus E_R, and tangential elastic modulus E_T, respectively. v_{12}, v_{13}, and v_{23} correspond to the tangential Poisson's ratio v_{RL}, radial Poisson's ratio v_{TL}, and longitudinal Poisson's ratio v_{RT}, respectively. G_{12}, G_{13}, G_{23} represent the longitudinal-radial shear modulus G_{RL}, longitudinal-tangential shear modulus G_{TL}, and radial-tangential shear modulus G_{RT}, respectively. The local coordinate system axes (1, 2, 3) must be strictly aligned with the global coordinate axes (Z, X, Y) when defining material parameters to ensure mechanical accuracy.

$$\begin{Bmatrix}\sigma_{11}\\ \sigma_{22}\\ \sigma_{33}\\ \sigma_{12}\\ \sigma_{23}\\ \sigma_{13}\end{Bmatrix} = \begin{bmatrix} 1/E_1 & -\nu_{21}/E_2 & -\nu_{31}/E_3 & 0 & 0 & 0 \\ -\nu_{12}/E_1 & 1/E_2 & -\nu_{32}/E_3 & 0 & 0 & 0 \\ -\nu_{13}/E_1 & -\nu_{23}/E_2 & 1/E_3 & 0 & 0 & 0 \\ 0 & 0 & 0 & 1/G_{12} & 0 & 0 \\ 0 & 0 & 0 & 0 & 1/G_{23} & 0 \\ 0 & 0 & 0 & 0 & 0 & 1/G_{13} \end{bmatrix}^{1} \begin{Bmatrix}\varepsilon_{11}\\ \varepsilon_{22}\\ \varepsilon_{33}\\ \gamma_{12}\\ \gamma_{23}\\ \gamma_{13}\end{Bmatrix} \quad (12)$$

E_1, E_2 and E_3 are the elastic moduli in the three orthogonal directions (MPa). G_{12}, G_{13} and G_{23} are the shear moduli on the 1–2, 1–3, and 2–3 planes (MPa), respectively. v_{ij} are the Poisson's ratios for the corresponding directional couplings. σ_{ij} are the stress components in specified directions (MPa). ε_{ij} are the principal strain components. γ_{ij} are the shear strain components.

(2) Plastic parameters of wood

This study employs the generalized Hill yield criterion within the ABAQUS Property module to define the plastic behavior of wood, which is given by:

$$\overline{\sigma} = \sqrt{F_{11}(\sigma_1-\sigma_2)^2 + F_{22}(\sigma_2-\sigma_3)^2 + F_{33}(\sigma_1-\sigma_3)^2 + 2N_{12}\tau_{12}^2 + 2N_{23}\tau_{23}^2 + 2N_{13}\tau_{13}^2} \quad (13)$$

$$F_{ii} = \left[\frac{(\sigma_0)^2}{2}\right]\left[\frac{1}{(\sigma_{kk})^2} + \frac{1}{(\sigma_{jj})^2} - \frac{1}{(\sigma_{ii})^2}\right] = \frac{1}{2}\left[\frac{1}{R_{kk}^2} + \frac{1}{R_{jj}^2} - \frac{1}{R_{ii}^2}\right](i \neq j \neq k = 1,2,3) \quad (14)$$

$$N_{ij} = \frac{3}{2}\left[\frac{\tau_0^2}{\tau_{ij}}\right] = \frac{3}{2}\left[\frac{1}{R_{ij}^2}\right](i \neq j = 1,2,3) \quad (15)$$

$$R_{ij} = \begin{cases} \overline{\sigma}_{ij}/\sigma_0 (i=j) \\ \overline{\sigma}_{ij}/\tau_0 (i \neq j) \end{cases} \quad (16)$$

The yield stress ratio calculation formulas are given as:

$$R_{11} = \overline{\sigma}_{11}/\sigma_0, R_{22} = \overline{\sigma}_{22}/\sigma_0, R_{33} = \overline{\sigma}_{33}/\sigma_0$$
$$R_{12} = \overline{\sigma}_{12}/\tau_0,\ R_{13} = \overline{\sigma}_{13}/\tau_0,\ R_{23} = \overline{\sigma}_{23}/\tau_0 \quad (17)$$

$$\tau_0 = \sigma_0 \Big/ \sqrt{3} \quad (18)$$

Published in: Engineering Structures (2026), vol. 352, 122134
DOI: 10.1016/j.engstruct.2026.122134
Statut: Postprint (Author's version)

where $\sigma_0$is the user-defined yield stress (MPa); $\bar{\sigma}_{ij}$ are the yield strength values in the principal directions (MPa); R_{ij} are the yield stress ratios in the principal directions.

Based on the aforementioned definitions and calculation methods for the elastic and plastic parameters of wood, and combined with the physical-mechanical properties of major tree species reported in Ref. [36], the elastoplastic parameters of larch, and Chinese fir are adopted for finite element simulations. The corresponding values are presented in Table 1, Table 2.

Table 1. Elastic parameters of wood (E_i and G_{ij} in MPa).

Classification	E_1	E_2	E_3	ν_{12}	ν_{13}	ν_{23}	G_{12}	G_{13}	G_{23}
Larch	15,642	1564.2	782.1	0.022	0.37	0.37	1173.15	938.52	281.556
White Poplar	10,780	1078	539	0.12	0.47	0.43	808.5	646.8	194.04
China Fir	10,340	1034	517	0.029	0.02	0.43	775.5	620.4	186.12

Table 2. Plastic parameters of wood.

Classification	R_{11}	R_{22}	R_{33}	R_{12}	R_{13}	R_{23}
Larch	1	0.11649	0.11649	0.23	0.055	0.23
White Poplar	1	0.113	0.113	0.307	0.076	0.307
China Fir	1	0.078	0.078	0.276	0.066	0.276

2.2.4. CFRP MATERIAL PROPERTIES

CFRP exhibits orthotropic mechanical properties as an anisotropic material of which stress-strain relationship is expressed as:

$$\sigma = \begin{cases} E_{\mathrm{f,cfrp}}\varepsilon_{\mathrm{f,cfrp}}(\varepsilon_{\mathrm{f,cfrp}} \le \varepsilon_{\mathrm{fu,cfrp}}) \\ 0(\varepsilon_{\mathrm{f,cfrp}} > \varepsilon_{\mathrm{fu,cfrp}}) \end{cases} \tag{19}$$

where $E_{\mathrm{f,cfrp}}$ is the elastic modulus of CFRP (MPa), $\varepsilon_{\mathrm{fu,cfrp}}$ is the ultimate tensile strain of CFRP, $f_{\mathrm{u,cfrp}}$ is the ultimate tensile strength of CFRP (MPa).

In ABAQUS, the elastic behavior of CFRP is defined using the Lamina method, since the material's performance predominantly depends on tensile characteristics along the fiber direction. The elastic material parameters are specified as: elastic modulus E_1 = 240 GPa (fiber direction), E_2 = 7.93 GPa (transverse direction), Poisson's ratio ν_{12} = 0.35, and shear moduli G_{12} = 5.3 GPa, G_{13} = 5.3 GPa, G_{23} = 4.0 GPa.

To simulate fracture behavior, the Hashin Damage model is employed via the Damage Evolution methodology. The failure parameters are defined as follows: longitudinal tensile strength X^T = 3227.4 MPa, longitudinal compressive strength X^C = 1414 MPa, transverse tensile strength Y^T = 37 MPa, transverse compressive strength Y^C = 169 MPa, longitudinal shear strength S_{12} = 134 MPa, and transverse shear strength S_{13} = 120 MPa.

2.2.5. MODELING STRATEGY AND CONFIGURATION

To accurately analyze the mechanical performance of concrete-filled steel tube composite columns with internally embedded CFRP-confined timber cores, a refined finite element model is established in ABAQUS. The sandwiched concrete, steel tubes, end plates, and timber cores are modeled using eight-node linear hexahedral reduced-integration elements (C3D8R) whilst CFRP is modeled using S4R shell elements. Since the end plates primarily undergo rigid displacement, they are simplified as rigid bodies by assigning infinitely large elastic moduli and near-zero Poisson's ratios, thereby eliminating

Published in: Engineering Structures (2026), vol. 352, 122134
DOI: 10.1016/j.engstruct.2026.122134
Statut: Postprint (Author's version)

deformation effects. For interfacial relationships, *Tie constraints are applied between end plates and steel tubes. Hard contact is used to simulate load transfer between end plates and concrete/timber cores, while preventing penetration. Hard contact criteria with Coulomb friction (μ = 0.6) in the tangential direction and critical shear stress τ_{bond} = 0.3 MPa is adopted to simulate the bond-slip effects between steel tube and concrete. Tie constraints are employed to present the CFRP-timber interfaces to ensure strain compatibility. Coulomb friction (μ = 0.4) is used to present the frictional slip behavior of CFRP-concrete interfaces. As illustrated in Fig. 6, the "critical regions receive mesh refinement" principle is followed, with denser grids in stress concentration zones and reduced density elsewhere to balance computational accuracy and efficiency. A fully fixed constraint is imposed on the reference point of the bottom end plate, while axial load is applied to the reference point of the top end plate using kinematic coupling constraints to associate the degrees of freedom of the end plate, thereby guaranteeing uniform load transfer.

Fig. 6. Model meshing of the composite column.

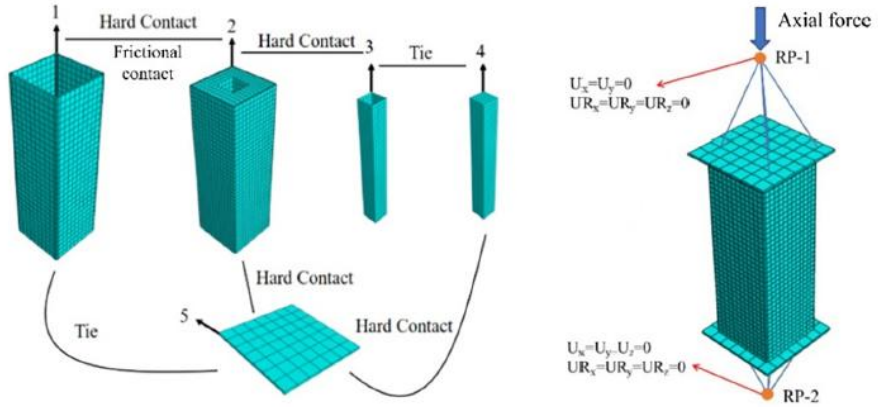

1. Steel tube 2. Concrete 3.CFRP 4. Timber core 5. End plates

2.3. MODEL VALIDATION

To verify the correctness of the finite element model for concrete-filled steel tube composite columns with internally embedded CFRP-confined timber cores, validations are conducted against the experimental data from Ref. [37] on concrete-filled steel tube stubs with embedded timber cores and Ref. [36] on CFRP-wrapped GLT timber columns.

2.3.1. VALIDATION AGAINST CFST WITH EMBEDDED TIMBER CORES

As described in Reference [37], all specimens in this study were circular concrete-filled steel tubular members. The specimens were divided into two groups based on the cross-sectional shape of the embedded timber core: square (STCS groups) and circular (STCC groups). Each group contained four specimens with different timber sizes, where the square timber had side lengths of 38, 54, 66, and 76 mm, and the circular timber had diameters of 43, 61, 74, and 86 mm, respectively. All specimens shared consistent basic parameters: the steel tube was made of Q235 steel, with a length of 420 mm and a wall thickness of 2 mm; the concrete was of grade C30; and the Mongolian Scotch pine timber had an average longitudinal compressive strength of 43.87 MPa and a longitudinal elastic modulus of

Published in: Engineering Structures (2026), vol. 352, 122134
DOI: 10.1016/j.engstruct.2026.122134
Statut: Postprint (Author's version)

11.9 GPa. The simulated load-displacement curves are shown in Fig. 7. The results demonstrate agreement between simulations and experimental outcomes, with overall curve shapes and stiffness characteristics closely matching. The calculated mean value of N_0/N is 0.980.

Fig. 7. Validation of axial load-displacement curves for composite columns with embedded circular timber cores.

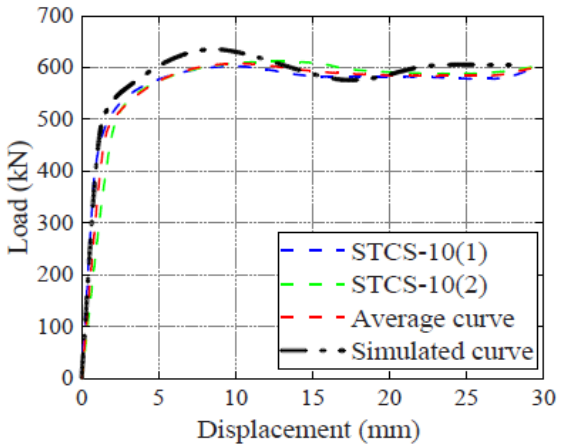

Fig. 8. Validation of axial load-displacement curves for CFRP-wrapped timber columns.

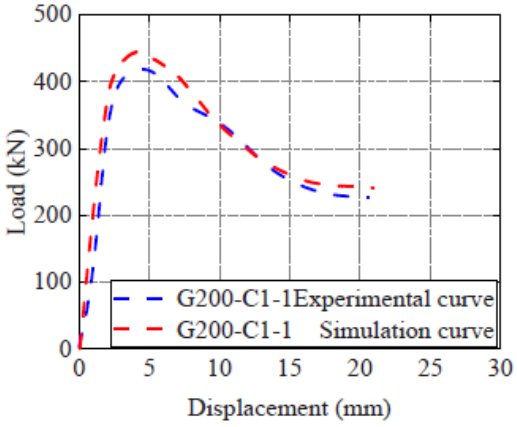

2.3.2. VALIDATION AGAINST CFRP-WRAPPED GLT TIMBER COLUMNS

A representative CFRP-wrapped timber column from Reference [38] is selected for validation. The specimens had cross-sectional dimensions of 105 mm × 105 mm with 10 mm fillet radii. Specimen G200-C1-1 had a height of 200 mm, while G400-C2-2 measured 400 mm. CFRP properties included a tensile strength of 3765.0 MPa, an elastic modulus of 227.9 GPa, and an ultimate strain of 0.019. Canadian hemlock dimension lumber was used, with a longitudinal compressive strength of 26.3 MPa, a longitudinal elastic modulus of 10.7671 GPa, and a density of 480 kg/m³. Finite element analysis modeling produced load-displacement curves are compared against experimental results, as shown in Fig. 8. The results reveal consistent variation trends and close alignment of fundamental stiffness. The mean N_0/N value is 0.962.

Published in: Engineering Structures (2026), vol. 352, 122134
DOI: 10.1016/j.engstruct.2026.122134
Statut: Postprint (Author's version)

3. Finite element simulation results

3.1. COMPARATIVE ANALYSIS OF FAILURE MODES

As shown in Fig. 9, conventional concrete-filled steel tube stubs under axial compression exhibit typical barreling failure modes, initiating at mid-height with concurrent steel tube local buckling and concrete crack propagation. In contrast, composite columns with internally embedded CFRP-confined timber cores demonstrate distinct failure mechanisms arising from material synergy. For square section, specimens with smaller timber cores display progressive buckling extending from the ends toward the mid-span, whereas specimens with larger timber cores concentrate failure at the ends while exhibiting enhanced deformation resistance. For circular sections, the failure mechanism depends on timber core geometry: specimens with circular cores show severe mid-span bulging, while those with square cores predominantly undergo shear failure. These results highlight the decisive influence of cross-sectional shape on failure mode evolution.

Fig. 9. Deformation of the tube and timber core.

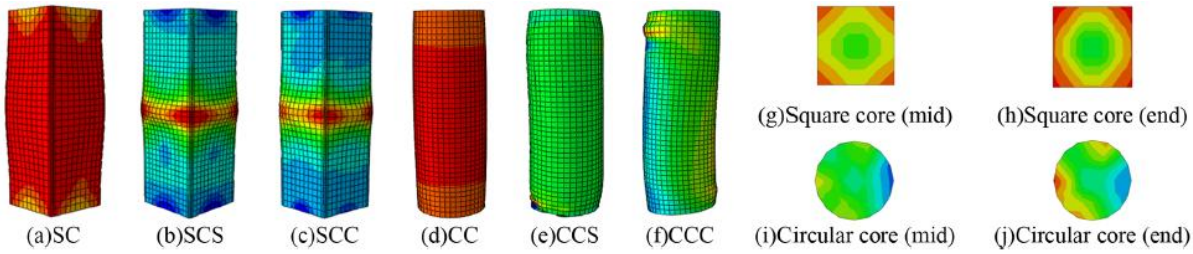

3.2. AXIAL LOAD-DISPLACEMENT CURVES

Fig. 10 examines the load distribution characteristics of the composite columns—SCS (Square tube-Concrete-Square timber core), CCC (Circular tube-Concrete-Circular timber core), CCS (Circular tube-Concrete-Square timber core), and SCC (Square tube-Concrete-Circular timber core). During the elastic phase, the steel tubes and concrete sustain the majority of the load, while the CFRP-confined timber cores carry only 1/7–1/5 of the total. Upon entering the elastoplastic phase, the timber core exhibits pronounced ductility under CFRP confinement, progressively increasing its load-sharing ratio to 1/3–1/2. Compared with conventional CFST, the composite columns show several advantages: CFRP confinement enables timber cores to retain 20–30% of residual bearing capacity post-crushing, significantly delaying strength degradation. Steel-concrete synergy enhances the peak bearing capacity by approximately 15–20%. Cross-sectional shape influences the overall bearing capacity by less than 5%. CFRP confinement efficiency is higher in circular timber cores, extending the ultimate displacement by 10–15% relative to square cores.

Published in: Engineering Structures (2026), vol. 352, 122134
DOI: 10.1016/j.engstruct.2026.122134
Statut: Postprint (Author's version)

Fig. 10. Load distribution in composite columns.

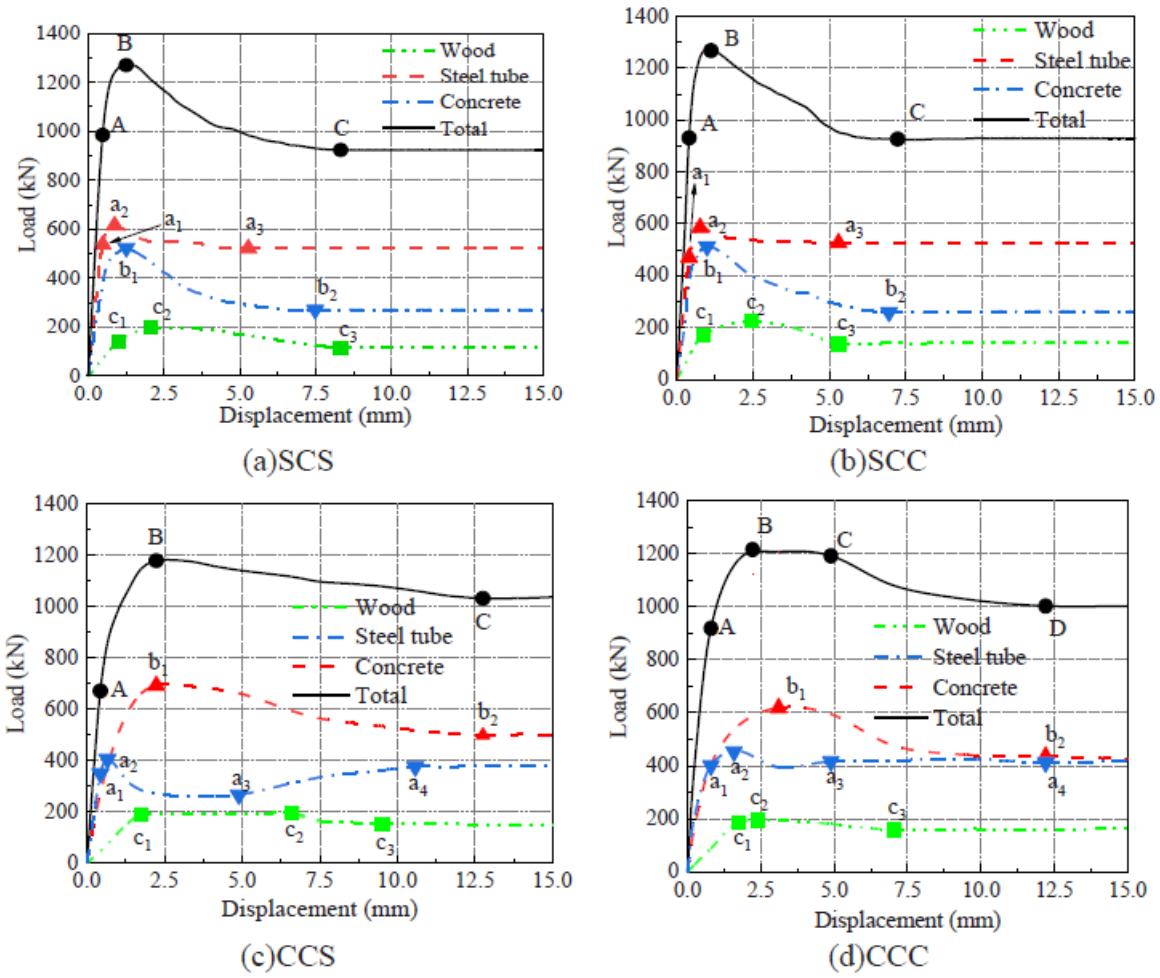

3.3. PARAMETRIC ANALYSIS

3.3.1. PARAMETER DESIGN

For square steel tube concrete control specimens, the column length is L = 450 mm, the steel tube outer side length is B = 150 mm, and the wall thickness is t = 4 mm. For circular steel tube concrete control specimens, the column length is L = 480 mm, the steel tube outer diameter is D = 160 mm, and the wall thickness is t = 4 mm. Both specimen types employ a concrete compressive strength of f_{cu} = 30 MPa and a steel yield strength of f_y = 235 MPa. The parametric analysis involves the effects of steel yield strength, concrete compressive strength, steel tube wall thickness, timber core dimensions, wood species, CFRP layer numbers, and CFRP tensile strength. The specific parameter values are provided in Table 3.

Published in: Engineering Structures (2026), vol. 352, 122134
DOI: 10.1016/j.engstruct.2026.122134
Statut: Postprint (Author's version)

Table 3. Specific parameter designs.

Parameter	Square Tubes	Circular Tubes
Steel Yield Strength (MPa)	235, 345, 390, 420	235, 345, 390, 420
Concrete Compressive Strength (MPa)	30, 40, 50, 60	30, 40, 50, 60
Tube Thickness (mm)	3, 4, 5, 6	3, 4, 5, 6
Square Timber Core (mm)	20, 40, 60, 80, 100	20, 40, 60, 80, 100
Circular Timber Core (mm)	22.5, 45.2, 67.6, 90.3, 112.8	22.5, 45.2, 67.6, 90.3, 112.8
Wood Species	Fir, Poplar, Larch	Fir, Poplar, Larch
CFRP Layer Numbers	2, 4, 6	2, 4, 6
CFRP Tensile Strength (MPa)	1000.0, 2000.0, 3227.4, 4000.0	1000.0, 2000.0, 3227.4, 4000.0

3.3.2. STEEL YIELD STRENGTH

The influence of steel yield strength on the load-displacement curves of SCS, SCC, CCS, and CCC composite columns is depicted in Fig. 11. All curves exhibit an initial ascending stage followed by a descending stage. With increasing steel yield strength, the peak loads increase significantly; however, the curves for high-strength steel display more pronounced brittle behavior in the descending phase.

Fig. 11. Influence of steel yield strength on load-displacement curves for composite columns.

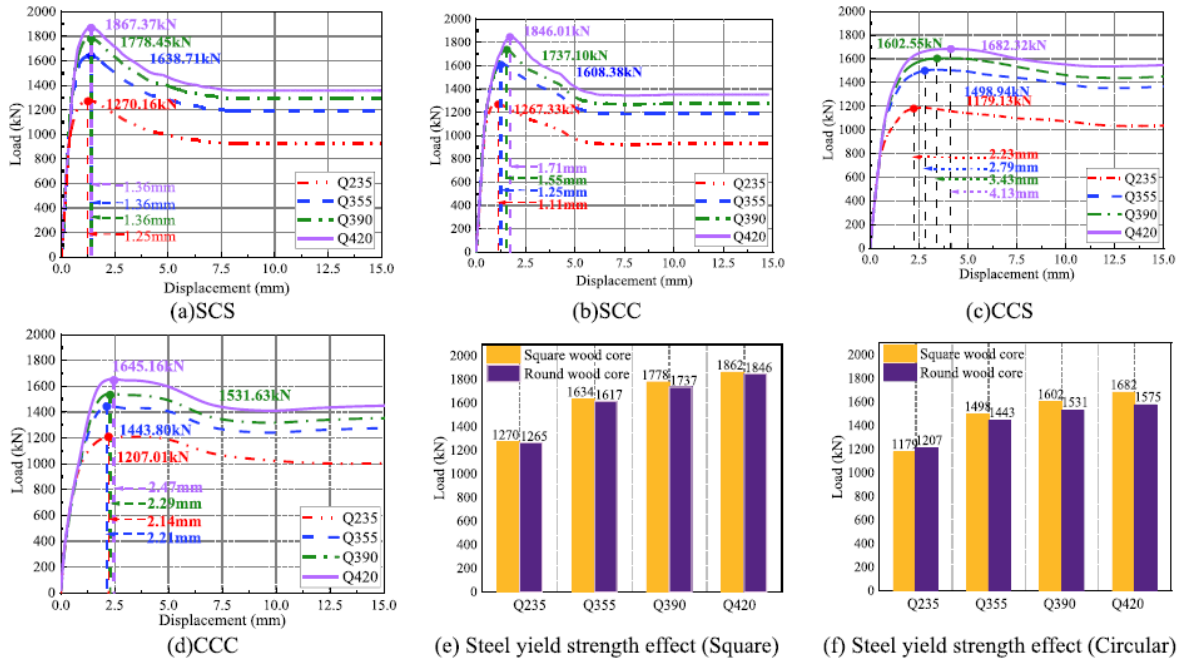

Fig. 11(e) and (f) present the ultimate bearing capacity of composite columns under varying steel yield strengths. The results demonstrate that both column types exhibit significant increases in ultimate bearing capacity with higher steel yield strengths, with square tube components showing more pronounced growth. Specifically, the composite columns with square tube achieve the ultimate bearing capacities ranging from 1270 to 1862 kN. The composite columns with circular tube achieve the ultimate bearing capacities ranging from 1179 to 1682 kN. Under identical steel strengths, the specimens with square timber cores as the cross-section of the square specimens is slightly larger than

Published in: Engineering Structures (2026), vol. 352, 122134
DOI: 10.1016/j.engstruct.2026.122134
Statut: Postprint (Author's version)

the circular ones and this difference cannot be compensated by the circumferential stresses which may develop in circular steel tubes.

3.3.3. CONCRETE COMPRESSIVE STRENGTH

Fig. 12 presents a comparative analysis of the influence of concrete compressive strength on the load-displacement curves of SCS, SCC, CCS, and CCC composite columns. With increasing concrete strength, the peak loads are increased significantly; however, the curves for high-strength concrete display steeper gradients in the descending phase, indicating reduced ductility. Square steel tube columns exhibit slightly greater bearing capacity enhancement compared with their circular tube counterparts.

Fig. 12. Influence of concrete strength on load-displacement curves of composite columns.

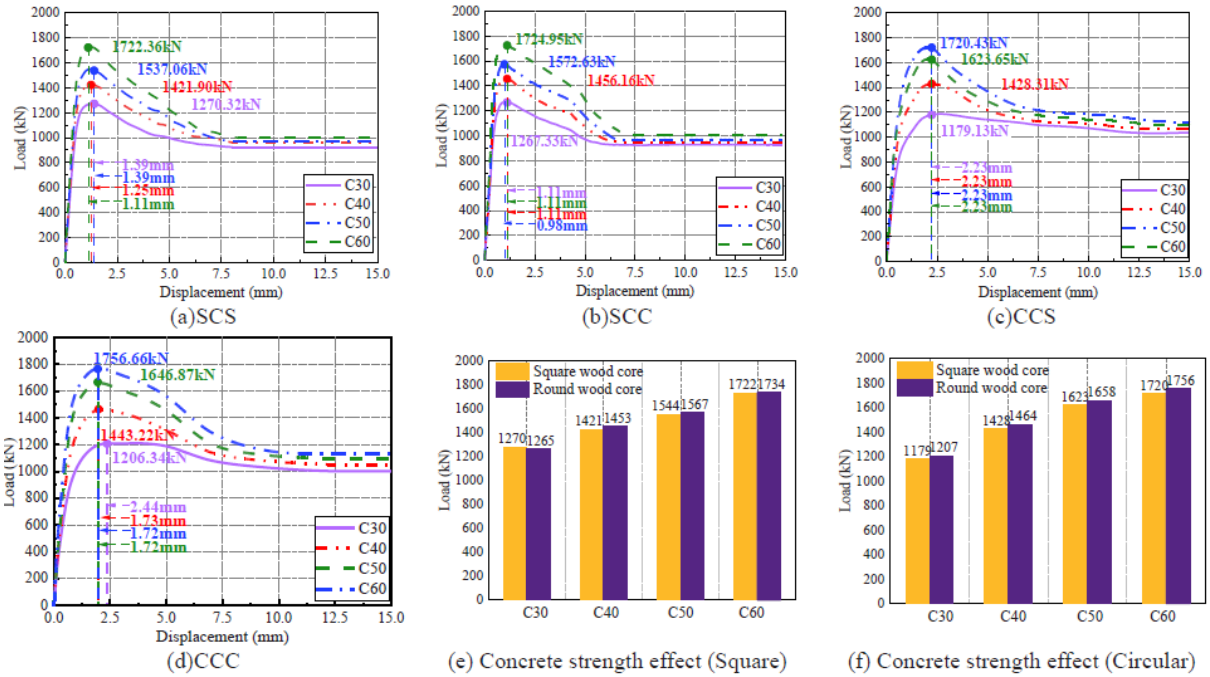

Fig. 12(e) and (f) present the ultimate bearing capacity of square and circular steel tube composite columns under different concrete strengths. The ultimate bearing capacities of both column types are increased significantly with higher concrete strength grades, with square tube ones exhibiting more pronounced enhancement. Under identical concrete strengths, specimens with square timber cores consistently achieve the higher ultimate bearing capacities than those with circular timber cores. The discrepancy between square and circular core specimens is widened as the concrete strength is increased.

3.3.4. WALL THICKNESS OF STEEL TUBES

Fig. 13 investigates the influence of steel tube wall thickness on the mechanical performance of SCS, SCC, CCS, and CCC composite columns. The load-displacement curves reveal that all composite columns exhibit typical elastoplastic deformation characteristics. With increasing wall thickness, the peak loads are increased significantly, and the descending phases of the curves become gentler, indicating that thicker-walled steel tubes effectively delay the structural failure of the columns. Square steel tube composite columns show greater bearing capacity enhancement than circular tube

Published in: Engineering Structures (2026), vol. 352, 122134
DOI: 10.1016/j.engstruct.2026.122134
Statut: Postprint (Author's version)

counterparts, confirming that increased wall thickness provides dual improvements in both bearing capacity and ductility for composite columns.

Fig. 13. Influence of steel tube wall thickness on load-displacement curves of composite columns.

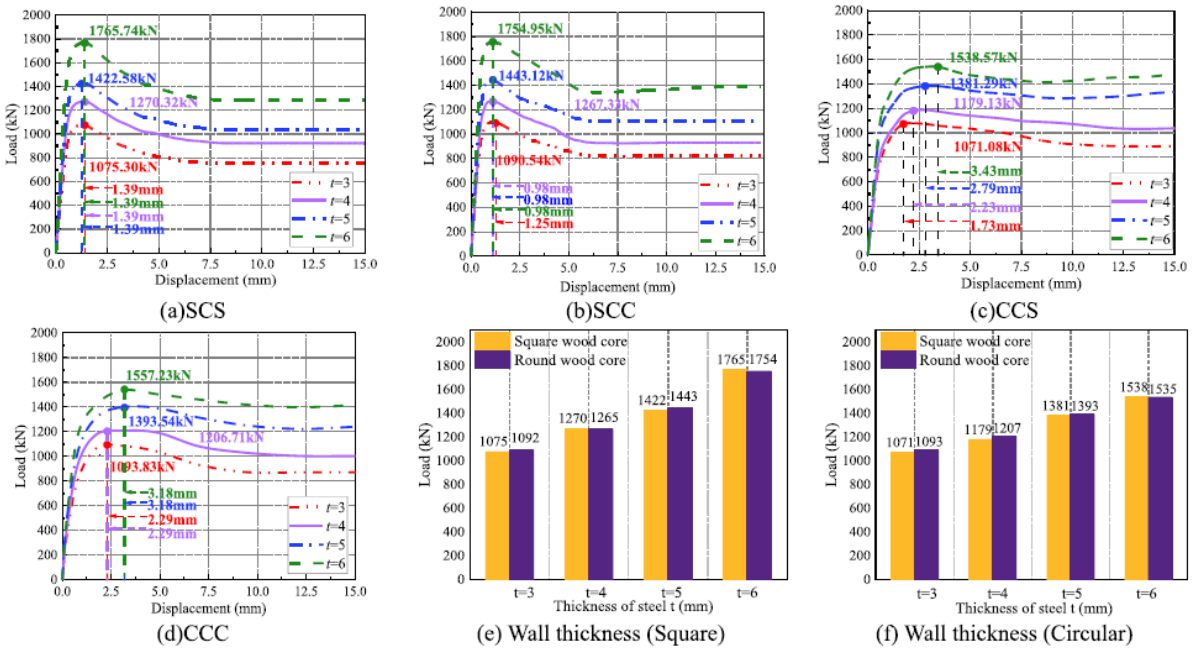

Fig. 13(e) and (f) present the influence of square steel tube wall thickness on the ultimate bearing capacity of composite columns. The ultimate bearing capacity of square timber core specimens is increased from 1075 kN to 1765 kN with greater wall thickness, representing a 64% enhancement, whilst that of the circular timber core specimens is increased from 1071 kN to 1538 kN, representing a 44% increase. Both datasets confirm that square timber core specimens consistently achieve higher ultimate bearing capacities than their circular timber core counterparts under identical conditions, with the performance gap progressively widening as wall thickness is increased.

3.3.5. TIMBER CORE DIMENSIONS

Fig. 14 comparatively analyzes the influence of timber cross-section dimensions on the load-displacement characteristics of SCS, SCC, CCS, and CCC composite columns. The results demonstrate that the peak loads of all composite columns are increased significantly with larger timber cross-section dimensions, with square timber core specimens exhibiting greater bearing capacity enhancement than circular timber core counterparts. The composite columns with larger timber sections show gentler descending phases after peak load attainment, indicating improved ductility.

Fig. 14(e) and (f) present the influence of timber cross-section dimensions on the ultimate bearing capacity of square and circular steel tube composite columns. The results demonstrate that the ultimate bearing capacities of both column types are increased significantly with larger timber cross-section dimensions. In square steel tube composites, specimens with square timber cores consistently achieve higher bearing capacities than those with circular timber cores, and this advantage amplified with increasing dimensions. In circular steel tube composites, the same trend is observed, but the difference in bearing capacity between square and circular timber cores is less pronounced.

Published in: Engineering Structures (2026), vol. 352, 122134
DOI: 10.1016/j.engstruct.2026.122134
Statut: Postprint (Author's version)

Fig. 14. Influence of timber cross-section dimensions on load-displacement curves of composite columns.

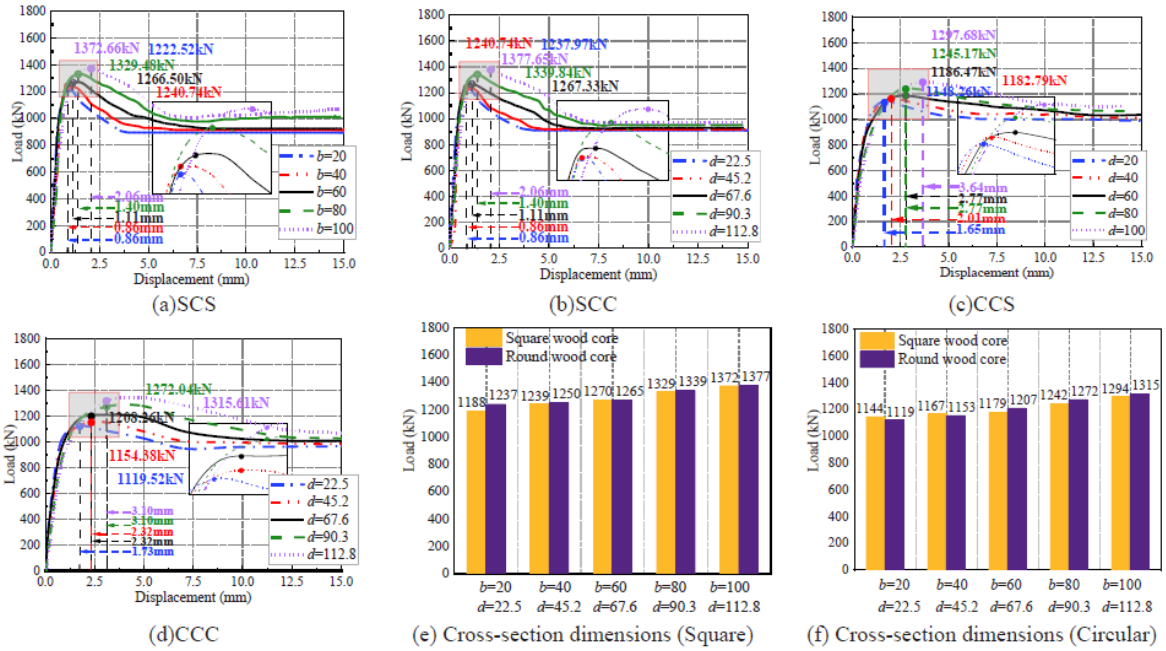

3.3.6. WOOD SPECIES

Fig. 15 investigates the influence of wood species on the mechanical performance of SCS, SCC, CCS, and CCC composite columns. All three wood species exhibit typical elastoplastic deformation characteristics, with larch specimens achieving the highest peak loads, followed by Chinese fir, and poplar showing the lowest values. All curves display gradual descending trends after peak load attainment, indicating that wood species primarily affect bearing capacity while exerting minimal influence on ductility. The bearing capacity of square steel tube composite columns is more affected by wood species than that of circular tube counterparts, confirming the coupling effect between timber mechanical properties and steel tube cross-sectional shape.

Fig. 15(e) and (f) present the ultimate bearing capacity performance of square and circular steel tube composite columns with Chinese fir, poplar, and larch. The results demonstrate that larch specimens achieve the highest bearing capacity in both square and circular tube systems, followed by poplar, with Chinese fir showing the lowest values. The disparity in bearing capacity among different wood species is more pronounced in square steel tube composites than circular tube systems. Square timber core specimens generally exhibit superior performance in square tubes, whereas this pattern reverses in circular tubes, where circular timber cores achieve higher bearing capacities.

3.3.7. CFRP LAYER NUMBERS

Fig. 16 analyzes the influence of CFRP layer numbers on the mechanical performance of SCS, SCC, CCS, and CCC composite columns. The results demonstrate that the peak loads of all composite columns are increased significantly with higher CFRP layer numbers, while the descending phases of the curves become progressively gentler. CFRP reinforcement simultaneously enhances both bearing capacity and ductility. Square steel tube composite columns exhibit much more pronounced load enhancement

Published in: Engineering Structures (2026), vol. 352, 122134
DOI: 10.1016/j.engstruct.2026.122134
Statut: Postprint (Author's version)

than circular tube counterparts, with square timber core specimens demonstrating optimal performance in SCS configurations.

Fig. 15. Influence of wood species on load-displacement curves of composite columns.

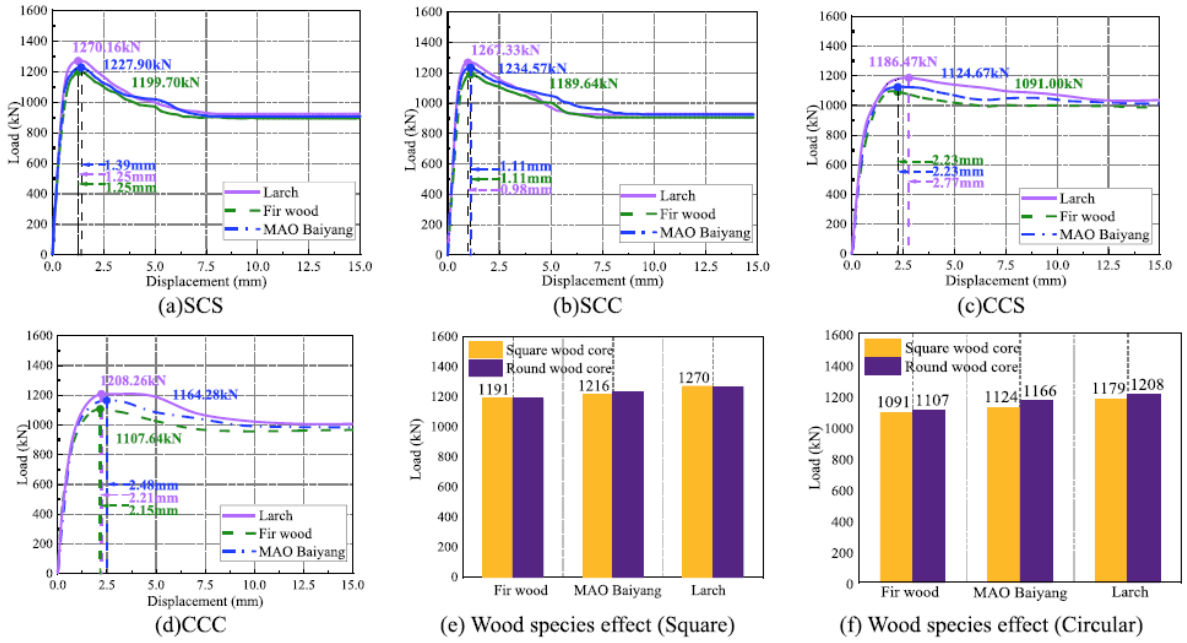

Fig. 16. Influence of CFRP layer numbers on load-displacement curves of composite columns.

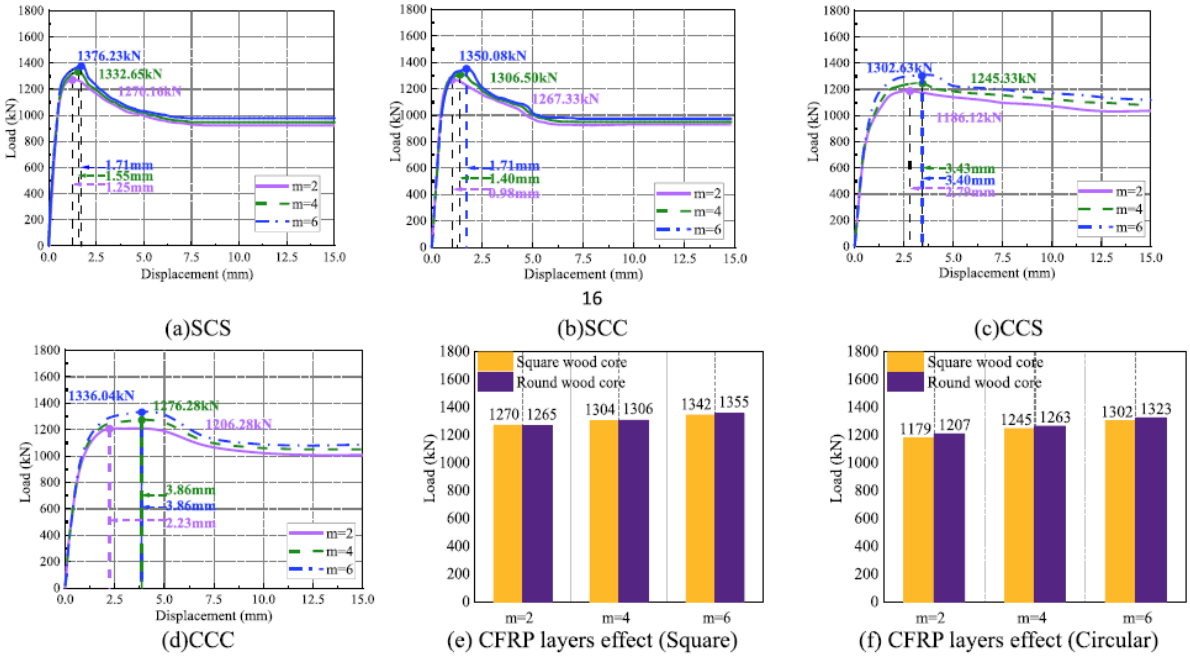

Fig. 16(e) and (f) analyze the influence of CFRP layer numbers on the ultimate bearing capacity of square and circular steel tube composite columns. The data reveal that the bearing capacities of both column types follow linear growth trends with increasing CFRP layer numbers, with square tube composites reaching peak values at m = 6 plies and circular tube composites achieving 1323 kN. Square timber core specimens show superior bearing capacities in square tubes only when m=2. In circular

Published in: Engineering Structures (2026), vol. 352, 122134
DOI: 10.1016/j.engstruct.2026.122134
Statut: Postprint (Author's version)

tubes, however, circular timber core specimens outperform square cores. These findings reveal synergistic interactions between CFRP enhancement and timber core geometry.

3.3.8. CFRP TENSILE STRENGTH

Fig. 17 analyzes the influence of CFRP tensile strength on load-displacement characteristics of the four composite column types. The results demonstrate that the peak loads of all composite columns are increased significantly with higher CFRP tensile strengths, while curves with high-strength CFRP exhibit gentler descending phases. This indicates that CFRP enhancement simultaneously improves both bearing capacity and ductility. Square steel tube composite columns show greater resistance enhancement than circular tube counterparts, with SCS specimens achieving the best overall performance.

Fig. 17. Influence of CFRP ply count on load-displacement curves of composite columns.

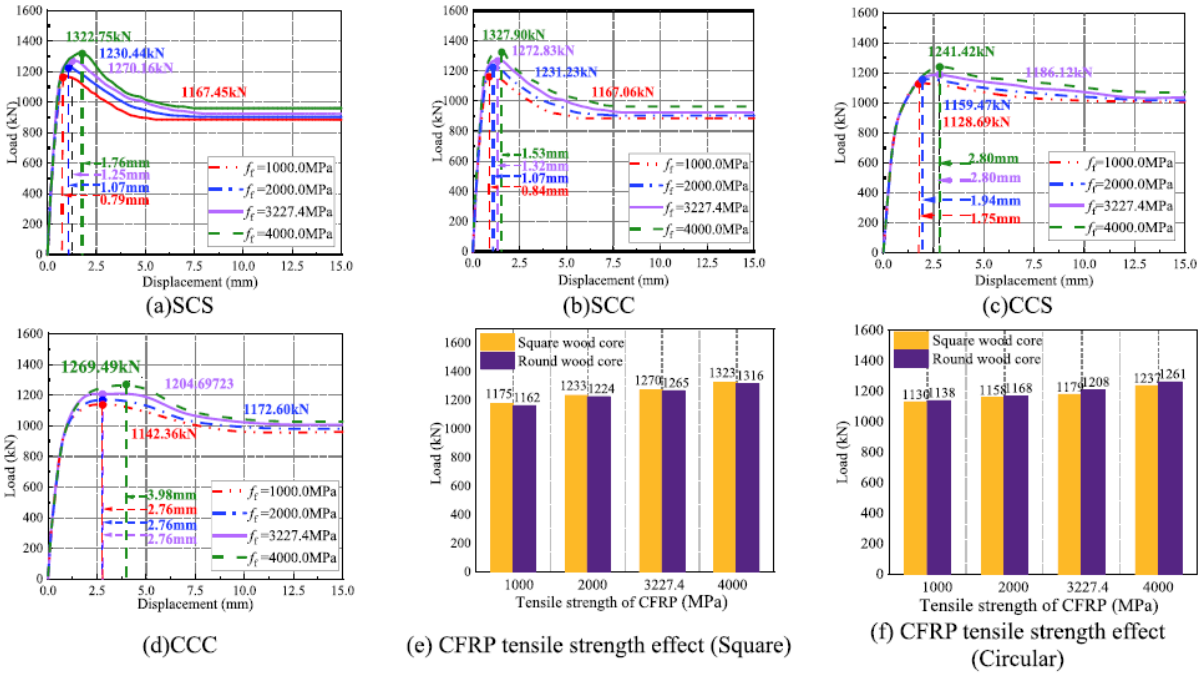

Fig. 17(e) and (f) present the influence of CFRP tensile strength on the ultimate bearing capacity of square and circular steel tube composite columns. The results demonstrate that the ultimate bearing capacities of both column types follow linear growth trends with increasing CFRP tensile strength, with square tube composites reaching approximately 1323 kN at 4000 MPa and circular tube composites achieving 1237 kN. In square tubes, square timber core specimens consistently achieve higher bearing capacities than circular core counterparts. In circular tubes, the difference between square and circular timber cores diminishes noticeably. These findings reveal synergistic interactions between CFRP enhancement and steel tube cross-sectional shape.

Published in: Engineering Structures (2026), vol. 352, 122134
DOI: 10.1016/j.engstruct.2026.122134
Statut: Postprint (Author's version)

4. Axial bearing capacity prediction method

4.1. PREDICTION ASSUMPTIONS

To derive the axial bearing capacity prediction method for concrete-filled steel tubular stubs with internally embedded CFRP-confined timber cores, the following fundamental assumptions are proposed to simplify the analysis of each component:

(1) Perfect bonding is assumed between the timber core and the CFRP outer layer, ensuring coordinated deformation among timber, CFRP, concrete, and steel tube, without separation during loading.

(2) The contribution of CFRP to axial load is neglected; CFRP is assumed to provide only hoop tensile stress in the fiber direction. For multi-layer CFRP, all layers are assumed to synchronously reach their ultimate state.

(3) Since the timber core diameter (or side length) is much larger than the CFRP thickness, the timber core diameter (or side length) is taken as approximately equal to the outer diameter (or side length) of the CFRP-confined timber core.

(4) Steel in tubes are idealized as elastic-perfectly plastic materials under triaxial stress, following von Mises yield criterion.

(5) Steel is assumed to exhibit distinct yield characteristics with identical tensile and compressive strength indices (tension-compression ratio α = 1). A parameter b = 0.5 is adopted, corresponding to the linear approximation of the Mises criterion.

Based on these assumptions, the ultimate bearing capacity of concrete-filled steel tubular stubs with internally embedded CFRP-confined timber cores is considered to comprise three components: the axial bearing capacity of the sandwiched concrete (N_c), the axial bearing capacity of the steel tube (N_{sp}), and the bearing capacity of the timber core (N_w) enhanced by CFRP and steel tube radial confinement. This relationship can be expressed as:

$$N_{up} = N_{sp} + N_c + N_w \tag{20}$$

4.2. BEARING CAPACITY CALCULATION FORMULAS

4.2.1. STRESS ANALYSIS OF STEEL TUBE

Based on the axisymmetric characteristics of circular steel tubes, the lateral confinement stress of the steel tube can be determined using thin-walled cylinder theory. When the Unified Strength Theory [39] is employed as the yield criterion for the tube wall, the lateral confinement stress p_c, acting on the steel tube wall under ultimate conditions, is expressed as:

$$p_c = \frac{f_y}{1-\alpha}\left[\left(\frac{R_0}{R_0+t}\right)^{\frac{2(1+b)(\alpha-1)}{2+2b-\alpha b}} - 1\right] \tag{21}$$

Published in: Engineering Structures (2026), vol. 352, 122134
DOI: 10.1016/j.engstruct.2026.122134
Statut: Postprint (Author's version)

where f_y is the yield strength of steel (MPa); R_0 is the internal diameter of the steel tube; t is the thickness of the steel tube wall (mm); α is the steel tensile-to-compressive strength ratio; $b(0 \le b \le 1)$ is the intermediate stress influence coefficient.

For conventional steels, compressive and tensile strengths can be considered approximately equivalent. By setting $\alpha = 1$ and $b = 0.5$, the linear approximation of the von Mises criterion is obtained:

$$p_c = 1.2 f_y 1n(R_0 + t) \Big/ R_0 \tag{22}$$

Based on the thick-walled cylinder theory, the axial compressive strength of the steel tube, σ_{sp}, is expressed as:

$$\sigma_{sp} = \frac{p_c R_0^2}{(R_0 + t)^2 - R_0^2} \tag{23}$$

The axial compressive bearing capacity of circular steel tubes, N_{sp}, is ultimately derived as:

$$N_{sp} = A_s \frac{p_c R_0^2}{(R_0 + t)^2 - R_0^2} \tag{24}$$

where A_s is the cross-sectional area of the steel tube (mm^2).

Using the cross-sectional area equivalence principle, the steel tube and concrete in composite columns are equivalently converted into those of a concrete-filled steel tube column. The calculation method is given as:

$$B^2 = \pi (R_e + t_e)^2 \tag{25}$$

$$(B - 2t)^2 = \pi R_e^2 \tag{26}$$

B is the width of the square steel tube (mm), R_e is the inner radius of the equivalent circular steel tube (mm), t_e is the wall thickness of the equivalent circular steel tube (mm). The equivalent parameters R_e and t_e can be derived from the following formulas:

$$R_e = (B - 2t) \Big/ \sqrt{\pi} = 0.5642(B - 2t) \tag{27}$$

$$t_e = 0.5642B - 0.5642(B - 2t) = 1.1284t \tag{28}$$

Due to the non-uniform confinement characteristics of square steel tubes on concrete, an equivalent confinement reduction factor ξ [40], which considers the wall thickness-to-width ratio $\lambda = t/B$, is introduced when converting square composite columns into equivalent circular columns, this treatment is also consistent with recent mechanism-based refinements for non-circular CFST confinement effects [19]:

$$\xi = 66.4741\lambda^2 - 0.9919\lambda + 0.41618 \tag{29}$$

The equivalent internal pressure of the concrete-filled equivalent circular steel tube is $p_e = p_s/\xi$, where p_e represents the equivalent uniform internal pressure exerted by the square steel tube on the core

Published in: Engineering Structures (2026), vol. 352, 122134
DOI: 10.1016/j.engstruct.2026.122134
Statut: Postprint (Author's version)

concrete. Under axial compression, the internal pressure within the equivalent concrete-filled circular steel tube is expressed as:

$$p_e = 1.2 f_y 1n \frac{R_e + t_e}{R_e} \tag{30}$$

Based on the thick-walled cylinder theory in plasticity mechanics, the following derivation is obtained:

$$\sigma_{sp} = \frac{p_s {R_e}^2}{(R_e + t_e)^2 - {R_e}^2} = \frac{\xi p_e {R_e}^2}{(R_e + t_e)^2 - {R_e}^2} \tag{31}$$

Finally, the axial compressive force borne by the square steel tube is derived as:

$$N_{sp} = A_s \frac{\xi p_e {R_e}^2}{(R_e + t_e)^2 - {R_e}^2} \tag{32}$$

4.2.2. STRESS ANALYSIS OF SANDWICHED CONCRETE

In the ultimate state, the stress condition of the sandwiched concrete satisfies $\sigma_3 < \sigma_1 = \sigma_2 < 0$, indicating triaxial compression. Employing the Twin-Shear Unified Strength Theory, the minor principal stress σ_3 can be expressed in terms of concrete cohesion c and internal friction angle φ as:

$$-\sigma_3 = \frac{2c \cos\varphi}{1 - \sin\varphi} - \frac{1 + \sin\varphi}{1 - \sin\varphi}\sigma_1 \tag{33}$$

When the concrete satisfies the Mohr-Coulomb criterion:

$$\frac{2c \cos\varphi}{1 - \sin\varphi} = f_{cc} \tag{34}$$

where f_{cc} is the uniaxial compressive strength of concrete (MPa).

By introducing the coefficient $k_c = (1 + \sin\varphi)/(1-\sin\varphi)$, the above relation simplifies to:

$$-\sigma_3 = f_{cc} - k_c \sigma_1 \tag{35}$$

Accordingly, the bearing capacity of concrete under steel tube confinement, σ_{cp}, is derived as:

$$\sigma_{cp} = f_c + kp \tag{36}$$

The internal pressure exerted by the steel tube on the concrete is denoted as p, where $p = p_c$ for circular steel tubes, $p = p_s$ for square steel tubes. Accordingly, the axial bearing capacity borne by the confined concrete is given by:

$$N_c = \sigma_{cp} A_c \tag{37}$$

where A_c is the concrete cross-sectional area (mm²).

4.2.3. STRESS ANALYSIS OF CFRP

Based on the principle of force equilibrium, the constraining force of CFRP can be derived as follows:

Published in: Engineering Structures (2026), vol. 352, 122134
DOI: 10.1016/j.engstruct.2026.122134
Statut: Postprint (Author's version)

For a circular cross-section:

$$\sigma_f = \frac{2mt_{cf}f_f}{d_w} \tag{38}$$

For a square cross-section:

$$\sigma_f = \frac{2mt_{cf}f_f}{b_w} \tag{39}$$

where m is the number of CFRP layers, f_f is CFRP tensile strength (MPa), t_{cf} is CFRP thickness (mm).

4.2.4. STRESS ANALYSIS OF TIMBER CORE

The timber core is subjected not only to CFRP confinement but also to constraining forces transmitted through the outer concrete from the surrounding steel tube. Accordingly, the total confining stress σ_T acting on the timber core is expressed as:

$$\sigma_T = \sigma_{ot} + \sigma_f \tag{40}$$

Depending on the cross-sectional configuration of both the steel tube and the timber core, the confinement stress σ_{ot} transmitted to the inner wooden core by the outer steel tube, via the confined concrete sandwich layer and the Carbon Fiber-Reinforced Polymer (CFRP), can be expressed as follows:

Square steel tube with square timber core:

$$\sigma_{ot} = p_s(R_e/b_w) \tag{41}$$

Square steel tube with circular timber core:

$$\sigma_{ot} = p_s(R_e/d_w) \tag{42}$$

Circular steel tube with circular timber core:

$$\sigma_{ot} = p_c(R/d_w) \tag{43}$$

Circular steel tube with square timber core:

$$\sigma_{ot} = p_c(R/b_w) \tag{44}$$

The ultimate strength models for FRP-confined timber columns can be generally summarized as follows [41], [42], [43], [44]:

$$\sigma_{wp}/f_w = 1 + k_w\left((\sigma_{ot} + \sigma_f)/f_w\right)^n \tag{45}$$

where k_w is the lateral pressure coefficient for the confined core timber column.

By substituting the corresponding datasets of the component groups (as established in the preceding sections) into Eq. (45) and conducting regression analysis, the axial compressive force undertaken by the timber core column is obtained as:

Published in: Engineering Structures (2026), vol. 352, 122134
DOI: 10.1016/j.engstruct.2026.122134
Statut: Postprint (Author's version)

$$N_w = A_w f_w \left[0.31\left(\left(\sigma_{ot} + \sigma_f\right)/f_w\right)^{0.72} + 1\right] \quad (46)$$

where A_w is the cross-sectional area of the timber core column (mm²).

Table 4. Summary of mechanistic equations.

Eq. nos.	Academic description	Section
(1)	Multi-regime elastoplastic constitutive representation for structural steel	2.2.1
(2)–(10)	Constitutive formulation for concrete in compression and tension, including key inputs for the damage-plasticity scheme	2.2.2
(11)	Idealized elastic-plastic law for timber under longitudinal compression	2.2.3
(12)	Orthotropic elastic compliance matrix describing timber anisotropic elasticity	2.2.3
(13)–(18)	Generalized Hill yield criterion and associated parameter definitions for timber plasticity	2.2.3
(19)	Linear-elastic brittle constitutive law for CFRP	2.2.4
(20)	Governing assumption for axial capacity superposition: steel tube + confined concrete + CFRP-enhanced timber core	4.2
(21)–(24)	Circular steel tube: derivation of lateral confining pressure and associated stress measures under axial compression	4.2.1
(25)–(28)	Equivalent circular transformation for square sections	4.2.1
(29)	Non-uniform confinement reduction factor for square steel tubes	4.2.1
(30)–(32)	Equivalent confining pressure and axial resistance expressions for square steel tubes via the equivalent-circular representation	4.2.1
(33)–(37)	Triaxial stress-state characterization and strength enhancement of the sandwiched confined concrete, integrating Twin-Shear Unified Strength Theory with Mohr–Coulomb-type failure considerations	4.2.2
(38)–(39)	CFRP hoop-confinement stress expressions for circular and square configurations	4.2.3
(40)	Resultant confinement stress acting on the timber core	4.2.4
(41)–(44)	Transferred confinement from the outer steel tube to the timber core through the concrete sandwich layer, specified for different cross-sectional combinations	4.2.4
(45)	Generalized ultimate-strength formulation for the confined timber core	4.2.4
(46)	Regression-calibrated final expression for axial resistance of the CFRP-confined timber core, accounting for synergistic confinement effects	4.2.4

Note: Equation numbering follows the manuscript sequence; page numbers correspond to the revised submission layout.

As summarized in Table 4, the mechanistic equations employed in this study are indexed by equation number together with their brief functions and corresponding sections.

4.2.5. VALIDATION OF BEARING CAPACITY CALCULATION FORMULA

The finite element analysis results (N) are compared against the calculated ones using the proposed formula (N_{up}), as illustrated in Fig. 18. For the composite columns with square steel tubes encasing CFRP-confined wooden cores, the average ratio of N/N_{up} is 1.03, while for those with circular steel tubes, the corresponding value is 0.96. To further confirm the applicability of the derived formula, the experimental data for steel-concrete-FRP-concrete specimens from Ref. [44] are employed for verification as shown in Fig. 19. This figure demonstrates strong consistency between the outcomes predicted by the modified design equation and those obtained from the FEA model.

Published in: Engineering Structures (2026), vol. 352, 122134
DOI: 10.1016/j.engstruct.2026.122134
Statut: Postprint (Author's version)

Fig. 18. Comparison between calculated values using the proposed equation and simulated values.

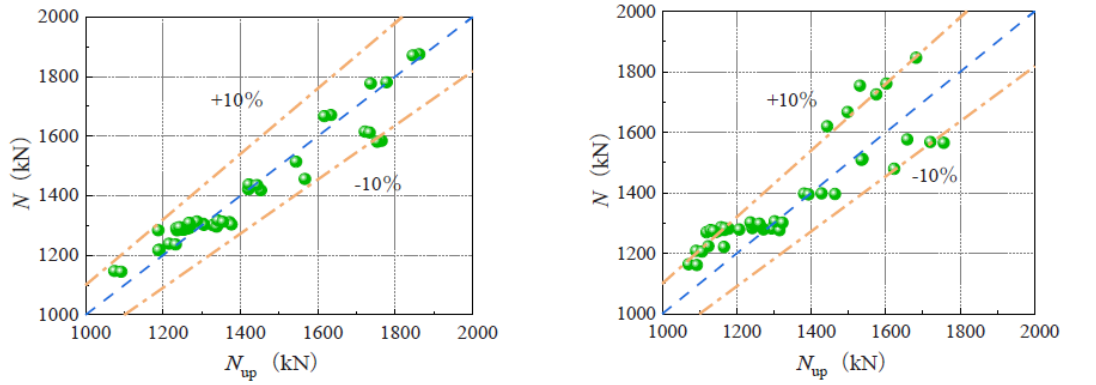

Fig. 19. Comparison between calculated values and experimental data from Ref. [42].

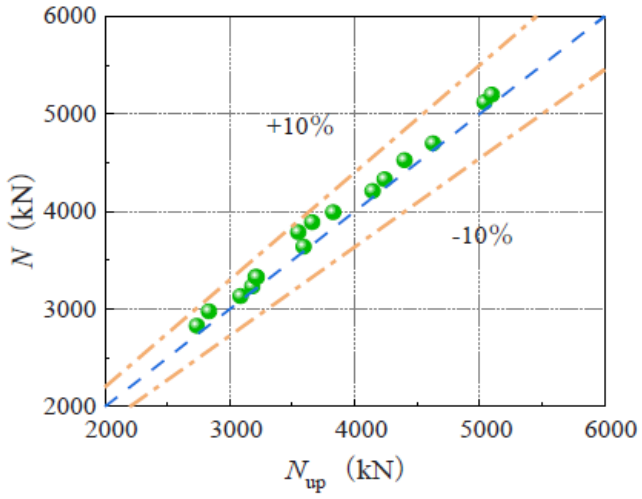

5. Machine learning prediction methods

5.1. MACHINE LEARNING FRAMEWORK

5.1.1. DATA ACQUISITION AND PREPROCESSING

The above analysis identifies the primary input features: tube shape, steel yield strength, concrete compressive strength, tube wall thickness, square timber core side length, circular timber core diameter, timber species, number of CFRP layers, and CFRP tensile strength. To satisfy the input requirements of machine learning algorithms, categorical variables are transformed using one-hot encoding, while continuous parameters preserve their full numerical precision. This preprocessing strategy improve the efficiency and stability of model training while ensuring the alignment with the theoretical parameter system derived from analytical formulations. A robust and consistent data foundation is established for the synergistic validation of finite element simulations and machine learning predictions.

Published in: Engineering Structures (2026), vol. 352, 122134
DOI: 10.1016/j.engstruct.2026.122134
Statut: Postprint (Author's version)

5.1.2. MODEL SELECTION

To determine the optimal predictive model for the ultimate compressive bearing capacity of steel tube-concrete-CFRP-timber composite stubs, a systematic comparison of ten machine learning algorithms is conducted. The architectures of these models are shown in Fig. 20. Specifically, the performance of XGBoost, MLP (Multi-layer Perceptron), KNN (K-Nearest Neighbors), GBDT (Gradient Boosting Decision Trees), AdaBoost (Adaptive Boosting), SVR (Support Vector Regression), Linear Regression, Random Forest, Ridge Regression, and Decision Tree is evaluated using five performance metrics [45], [46], [47]. For clarity of visualization, MSE (Mean Squared Error) values are scaled by a factor of 0.1, while R^2 (Coefficient of Determination) values are multiplied by 10 in Fig. 21. Comparative analysis demonstrates that the Decision Tree model achieves the highest predictive performance, with an R^2 value of 0.82955, significantly outperforming other models, particularly the lowest-performing KNN. Regarding error metrics, KNN exhibits the largest MSE and MAPE (Mean Absolute Percentage Error), whereas the Decision Tree and Ridge Regression models achieve more favorable trade-offs, maintaining MSE values between 10 and 15, and MAPE values below 4%. As shown in Fig. 21, although the Decision Tree attains the highest R^2, its relatively elevated MAPE suggests sensitivity to outliers. In contrast, ensemble learning methods (XGBoost, Random Forest) demonstrate consistently strong predictive accuracy, though at the cost of higher computational complexity. These findings offer critical guidance for balancing predictive accuracy and computational efficiency in engineering practice.

Fig. 20. Architectures of the ten machine learning models.

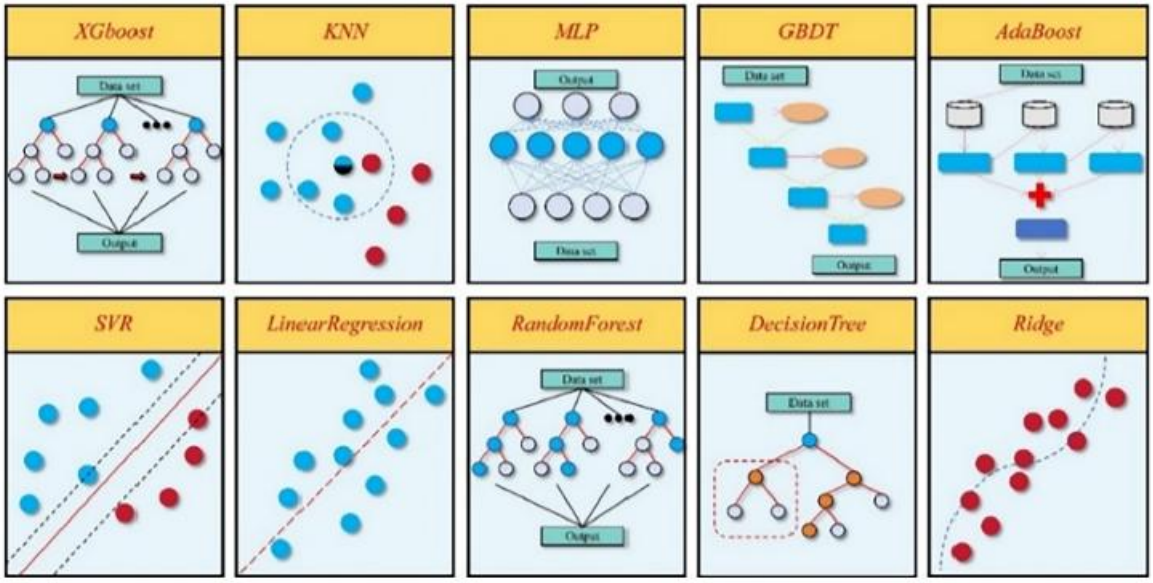

Published in: Engineering Structures (2026), vol. 352, 122134
DOI: 10.1016/j.engstruct.2026.122134
Statut: Postprint (Author's version)

Fig. 21. Performance of the models across five key metrics.

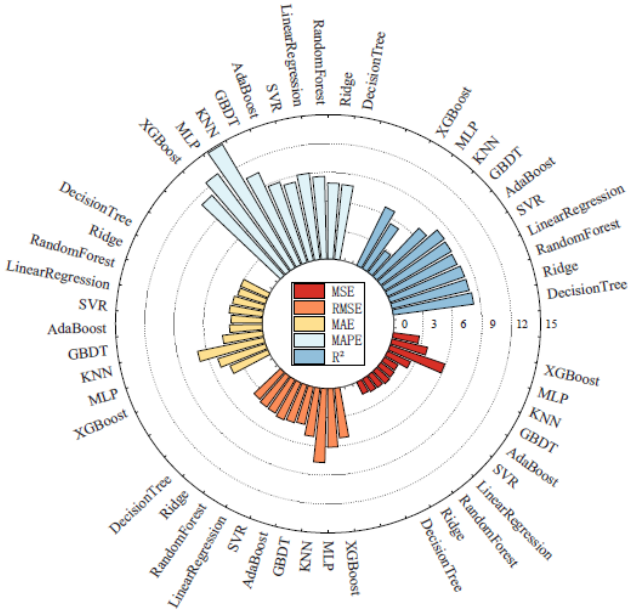

5.1.3. MODEL TRAINING

To ensure robustness and reproducibility of the prediction results, this study adopts a rigorous model training framework. The dataset is divided into training and test subsets using a 7:3 ratio, where the training set is employed to optimize model parameters and the test set is reserved for final evaluation. A repeated 5-fold cross-validation strategy with 10 iterations is utilized to reduce random fluctuations and maximize data utilization. Hyperparameter optimization is conducted using a randomized search for computational efficiency, exploring constrained parameter spaces. Specifically: XGBoost explores subsample values [0.6–1.0], yielding an optimal configuration of subsample = 1.0 and max_depth = 7; Random Forest explores n_estimators [50–200], with optimal parameters n_estimators = 150 and max_depth = 5. For MLP, overfitting is mitigated via learning rate adjustment (0.01) and a 100-neuron hidden layer, while KNN explores distance-based weighting (weights='distance') with Manhattan distance (p = 1). A fixed random seed is enforced to ensure full reproducibility, and all models are trained under identical hardware and software conditions to maintain fair benchmarking. This systematic training methodology enhances generalizability and establishes a robust foundation for comparative performance analysis as listed in Table 5.

Table 5. Optimal hyperparameters of the ten machine learning models.

Models	Optimal hyperparameters
XGBoost	{'subsample': 1.0, 'n_estimators': 150, 'max_depth': 7, 'learning_rate': 0.2, 'colsample_bytree': 0.6}
MLP	{'mlp__learning_rate_init': 0.01, 'mlp__hidden_layer_sizes': (100,), 'mlp__alpha': 0.01, 'mlp__activation': 'relu'}
KNN	{'weights': 'distance', 'p': 1, 'n_neighbors': 7}
GBDT	{'n_estimators': 100, 'min_samples_split': 10, 'max_depth': 3, 'learning_rate': 0.1}
AdaBoost	{'n_estimators': 50, 'loss': 'linear', 'learning_rate': 1.0}
SVR	{'kernel': 'linear', 'epsilon': 0.5, 'C': 0.1}
LinearRegression	{'Without parameter tuning': 'None'}
RandomForest	{'n_estimators': 150, 'min_samples_split': 5, 'min_samples_leaf': 1, 'max_depth': 5}
Ridge	{'solver': 'sparse_cg', 'alpha': 10.0}
DecisionTree	{'min_samples_split': 2, 'min_samples_leaf': 4, 'max_depth': 5}

Published in: Engineering Structures (2026), vol. 352, 122134
DOI: 10.1016/j.engstruct.2026.122134
Statut: Postprint (Author's version)

5.2. MACHINE LEARNING PREDICTION RESULTS

5.2.1. BEARING CAPACITY

Comprehensive analysis of predictions from the ten machine learning models in Fig. 22 reveals that the Decision Tree (j) and Ridge Regression (i) models achieve the most favorable overall performance. The Decision Tree exhibits near-perfect alignment between predicted and observed values in the test set, particularly within the bearing capacity range of 20–40 kN, where the curves almost entirely overlap. Its prediction variance is substantially smaller than that of other models. The Ridge Regression model demonstrates outstanding stability, with its prediction curve closely following the observed values across the entire parameter domain. Its accuracy at extreme bearing capacities surpasses more complex models such as XGBoost and MLP, reflecting the overfitting-mitigating benefits of its L2 regularization. Both models exhibit minimal discrepancies between training and test set performance, underscoring their superior generalization capabilities relative to other algorithms.

In contrast, while XGBoost (a) and Random Forest (h) demonstrate strong fitting performance on the training data, their test-set predictions reveal systematic deviations at critical bearing capacities. Models such as KNN (c) and SVR (f) exhibit excessive prediction volatility, undermining their reliability. This performance divergence underscores that, for engineering problems characterized by pronounced material nonlinearity (e.g., steel tube-concrete-CFRP-timber stub columns), moderately complex models such as Decision Tree and regularized linear approaches such as Ridge Regression strike the most effective balance between predictive accuracy and computational efficiency.

Fig. 22. Prediction accuracy of ten models across datasets.

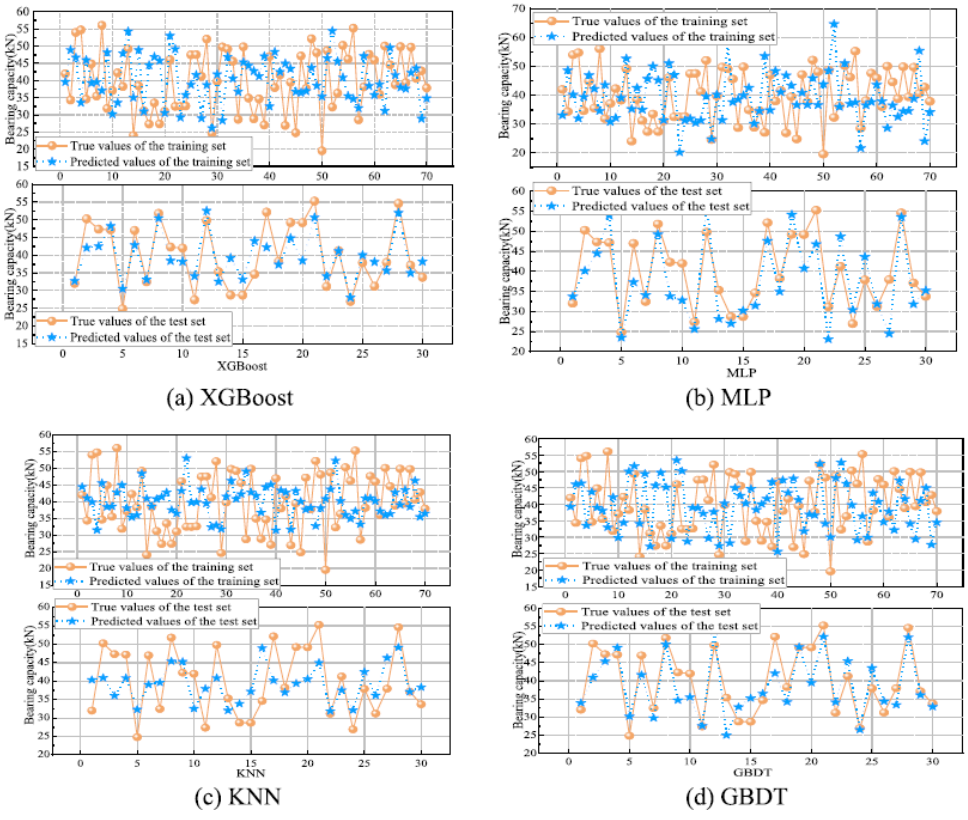

(a) XGBoost (b) MLP

(c) KNN (d) GBDT

Published in: Engineering Structures (2026), vol. 352, 122134
DOI: 10.1016/j.engstruct.2026.122134
Statut: Postprint (Author's version)

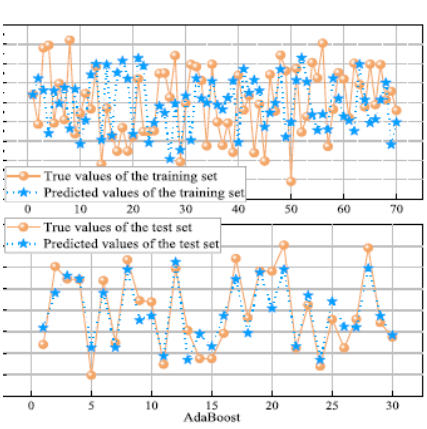

(e) AdaBoost

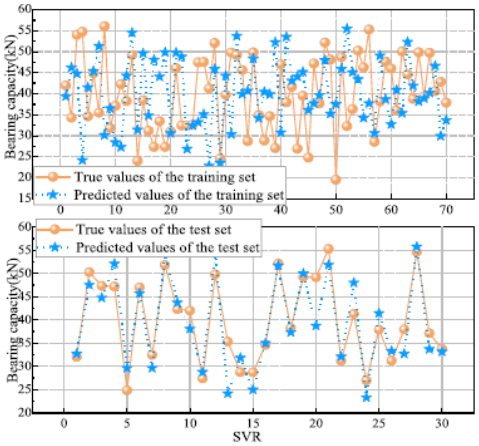

(f) SVR

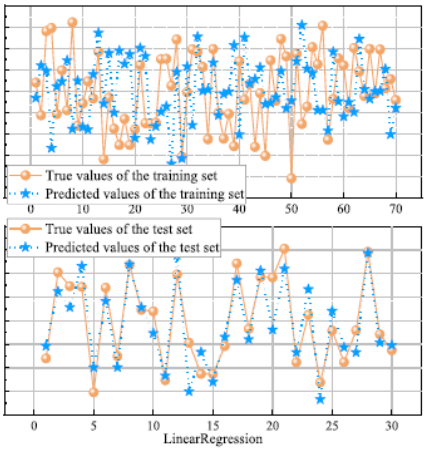

(g) LinearRegression

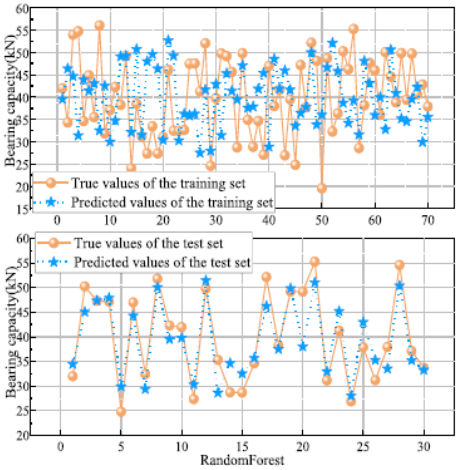

(h) RandomForest

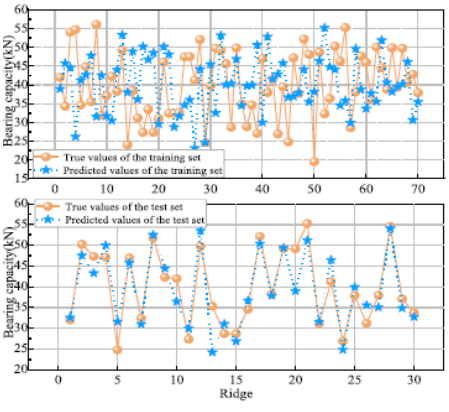

(i) Ridge

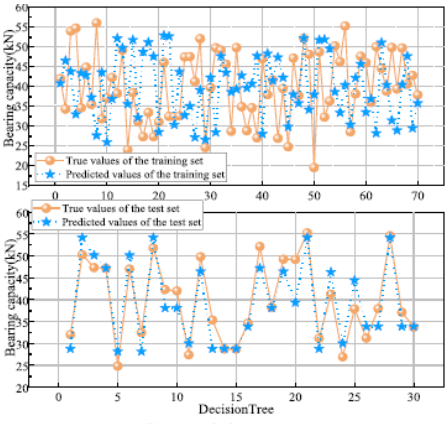

(j) DecisionTree

From an error-distribution perspective, linear models maintain stable predictive performance, with only minor deviations between test-set predictions and ground truth values. This finding suggests that simple linear relationships are sufficient to capture the primary trends in the dataset for practical engineering applications. Conversely, boosting-based algorithms such as AdaBoost (e) and GBDT (d) display clear signs of overfitting on the training data, systematically underestimating bearing capacities at the higher-load ranges. Visual comparisons of all models' outputs confirm that model performance depends not only on algorithm selection but also on hyperparameter tuning, feature representation

Published in: Engineering Structures (2026), vol. 352, 122134
DOI: 10.1016/j.engstruct.2026.122134
Statut: Postprint (Author's version)

quality, and outlier robustness, offering concrete directions for future optimization of predictive frameworks.

5.2.2. PARAMETER ANALYSIS

Building upon the preceding results, this study narrows its focus to the four best-performing machine learning models. Feature-importance analysis using SHAP (SHapley Additive exPlanations) values (Fig. 23) reveal clear differences in the relative contributions of material parameters toward predicting the ultimate compressive bearing capacity of composite stub columns. These figures visualize SHAP-based importance rankings for XGBoost (a), Random Forest (b), Decision Tree (c), and AdaBoost (d). All plots adopt uniform conventions: the horizontal axis represents SHAP value magnitude, the vertical axis lists input features including concrete compressive strength, steel yield strength, timber species, timber core size, CFRP tensile strength, number of CFRP layers, steel tube type, and steel tube wall thickness, and point coloration corresponds to normalize feature values. Across all four models, concrete compressive strength and steel yield strength consistently produce the highest SHAP values, confirming their dominant role in shaping predictive outcomes. In contrast, timber-related features and CFRP layer numbers exhibit dispersed SHAP distributions, suggesting model-dependent contributions. Steel tube type and wall thickness consistently demonstrate minimal SHAP values, highlighting their marginal effect on prediction. A noteworthy observation is that Random Forest (b) displayed narrower SHAP ranges than the other models, a result is attributable to ensemble averaging that mitigates extreme feature effects and produces more concentrated SHAP clustering. While feature-importance rankings vary slightly among algorithms, the primacy of core material properties (concrete and steel) remains unequivocal.

Fig. 23. Importance of SHAP features.

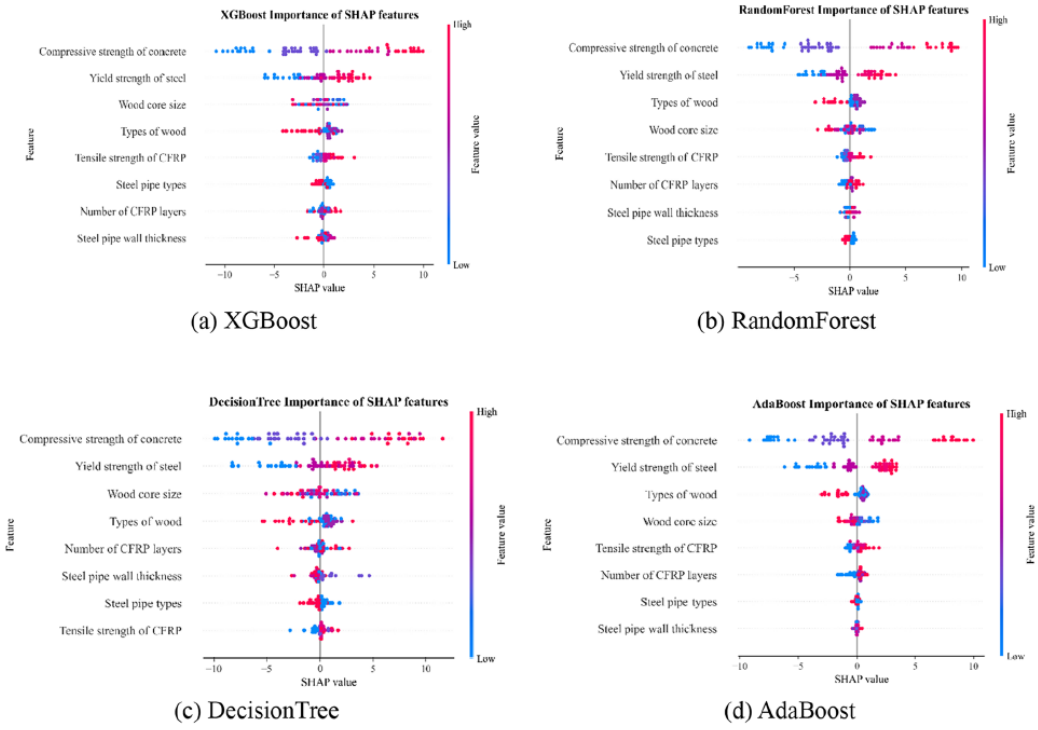

(a) XGBoost (b) RandomForest

(c) DecisionTree (d) AdaBoost

Published in: Engineering Structures (2026), vol. 352, 122134
DOI: 10.1016/j.engstruct.2026.122134
Statut: Postprint (Author's version)

Fig. 24 visualizes how each material parameter shifts the predicted capacity within the trained ML model: concrete strength shows the widest SHAP range and thus the strongest overall contribution; steel yield strength exhibits a distinct nonlinear influence with a peak contribution around 300 MPa; CFRP-related variables show more conditional effects (dispersed contributions for layer number and limited sensitivity to tensile strength); steel-tube geometry presents threshold-like responses for wall thickness and relatively symmetric contributions for tube type; timber variables provide secondary but non-negligible effects, with concentrated positive contributions for core sizes around 60–80 mm. The red zero line indicates neutral contribution and the gray density band reflects the data distribution.

Fig. 24. Comprehensive SHAP value analysis of material properties in structural performance prediction.

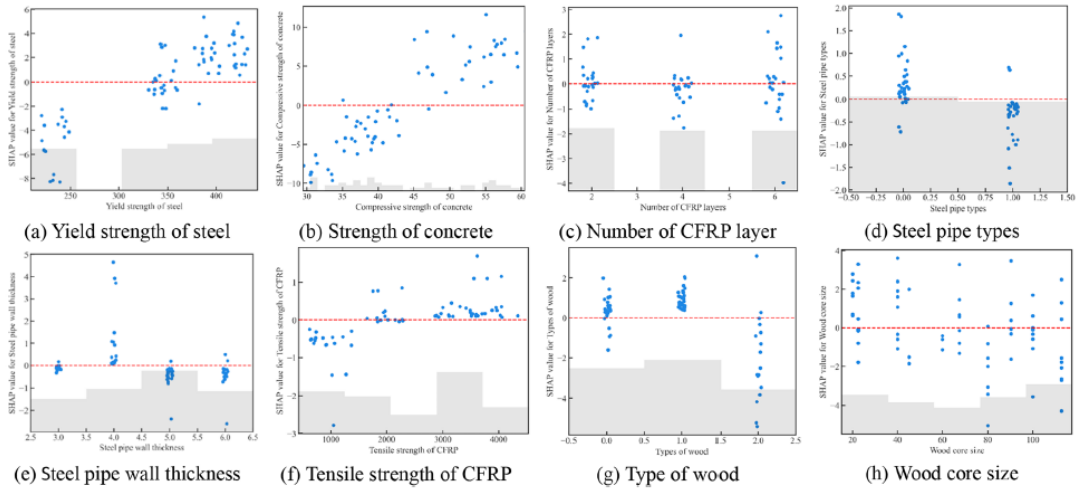

5.3. TRM-XGBOOST MODEL

To further substantiate the applicability of machine learning in predicting the axial compressive behavior of concrete-filled steel tubular columns incorporating CFRP-confined timber cores, this study integrates the theoretical formulation with SHAP value analysis to establish a novel TRM-XGBoost (Theoretical-Residual Modified XGBoost) prediction framework.

Although the Decision Tree model previously achieves a strong R^2 value of 0.82955, its inherent limitations as a single-learner algorithm restrict its capacity to capture the highly nonlinear and coupled interactions governing composite column behavior. Decision Trees are prone to instability with small perturbations in training data and are sensitive to noise, which can compromise generalization for critical behaviors such as nonlinear peak responses and the dispersed SHAP patterns associated with CFRP ply counts.

Notably, the selection of XGBoost as the base model for TRM development is not solely determined by whether a competing model achieved a marginally higher score on a single metric. Instead, XGBoost is chosen because it offers the best balance between prediction accuracy, stability, and compatibility with theory-guided residual correction. As an ensemble gradient-boosting method, XGBoost reduces variance by aggregating multiple weak learners and provides strong regularization, leading to more reliable performance across different data splits. More importantly, the TRM strategy requires a base learner whose residuals are structured and learnable after subtracting theoretical predictions; XGBoost is particularly effective at modeling such residual patterns with mixed continuous inputs and

Published in: Engineering Structures (2026), vol. 352, 122134
DOI: 10.1016/j.engstruct.2026.122134
Statut: Postprint (Author's version)

monotonic-like trends without intensive feature engineering. In addition, XGBoost integrates naturally with SHAP for consistent interpretability and enables efficient training and deployment, making it more suitable than less stable single learners or computationally heavier alternatives for the proposed full-chain framework.

The proposed TRM-XGBoost framework employs SHAP-guided feature attention mechanisms to implement fine-grained residual corrections to theoretical predictions, thereby harnessing the synergistic strengths of mechanical theory and machine learning. While the conventional theoretical formulation (Eq. 20) retains strong physical interpretability, it exhibits inherent biases in capturing composite synergy effects and sensitivity to boundary conditions. Through XGBoost's feature-attention capability, the TRM-XGBoost model adaptively emphasizes dominant contribution variables (e.g., concrete compressive strength) and critical thresholds (e.g., CFRP layer numbers), thereby enabling locally weighted residual corrections. This strategy not only preserves the interpretability of theoretical formulations but also compensates for higher-order nonlinear effects via data-driven learning. As a result, the model achieves a substantial performance breakthrough, improving R^2 from 0.82955 to 0.9873.

The TRM-XGBoost architecture adopts a dual-stage hybrid design. Eq. (20) is first applied to each sample to compute a mechanics-based baseline capacity by summing the contributions of the confined concrete, steel tube, and CFRP–timber core. This baseline is then compared with the corresponding FE capacity to obtain a "theory–FE residual" (i.e., the remaining error not captured by the theoretical formulation). Next, an XGBoost model is trained to learn this residual using the same input parameters together with the theory-based baseline as additional information. After training, prediction proceeds in two steps: (1) calculate the baseline capacity from Eq. (20); and (2) let the residual model output a correction term, which is added to the baseline to obtain the final capacity prediction. SHAP is employed only on the residual model to identify which variables consistently drive the residual; these SHAP-ranked features are then used to guide the residual-learning emphasis, ensuring the correction targets systematic theory mismatch rather than noise.

Fig. 25. Feature contribution map of the TRM-XGBoost model.

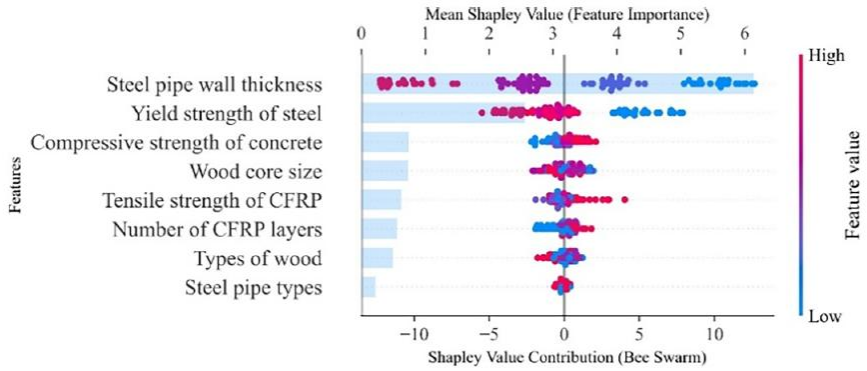

As revealed by the SHAP-based feature importance analysis in Fig. 25, steel tube wall thickness, steel yield strength, and concrete compressive strength emerge as the dominant parameters controlling axial bearing capacity—directly corroborating the conclusions reported in Section 2.3. This outcome not only highlights the critical parameter intervals that require prioritized residual correction but also provides a cross-validation of earlier finite element simulation results. Prediction performance scatter

Published in: Engineering Structures (2026), vol. 352, 122134
DOI: 10.1016/j.engstruct.2026.122134
Statut: Postprint (Author's version)

plots (Fig. 26) further demonstrate that data points are densely clustered within the ±10% error margin, with the TRM-XGBoost model achieving an R^2 of 0.9873. These findings confirm that TRM-XGBoost accurately captures the global influence of dominant factors such as concrete compressive strength, while simultaneously correcting localized prediction deviations in sensitive regions (e.g., timber core sizes between 60–80 mm and discretely distributed CFRP ply counts) through its residual correction mechanism. Collectively, this establishes TRM-XGBoost as a highly effective integration of theoretical formulations with machine learning methodologies, offering both interpretability and predictive robustness.

Fig. 26. Accuracy of the TRM-XGBoost model.

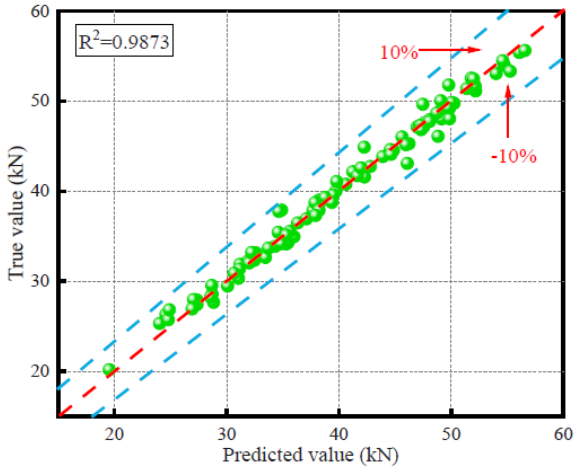

5.4. LIGHTWEIGHT COMPOSITE COLUMN DESIGN PROGRAM

Accurate prediction of axial compressive bearing capacity is essential for ensuring structural safety, reliability, and efficient resource utilization in engineering practice. Traditional methods, which often rely on simplified empirical formulas and omit comprehensive parametric sensitivity analysis, provided the motivation for developing a lightweight prediction software package (included in the Supplementary materials). As shown in Fig. 27, the user interface integrates the proposed TRM-XGBoost algorithm as its computational core, thereby combining the theoretical rigor of mechanics-based formulations with the predictive precision of machine learning. This software substantially reduces manual calculation errors and delivers a practical decision-support tool aligned with contemporary engineering requirements for rapid, accurate, and reliable bearing capacity evaluation.

The software interface adopts a dual-column layout. Functionally, users upload standardized Excel datasets through an interactive input module, after which the TRM-XGBoost prediction engine, augmented with feature-attention mechanisms, automatically generates numbered bearing capacity outputs. The left-hand panel functions as the primary data input and interaction zone (Fig. 28). Its upper section enables batch uploads, while the lower section provides single-instance prediction with horizontal column graphics serving as visual anchors. Users sequentially input eight engineering variables (steel tube, concrete, timber core, CFRP parameters) through component-specific buttons, with individual predictions triggered once combined component data are saved. The system then returns both axial bearing capacity and component self-weight, calculated automatically according to

Published in: Engineering Structures (2026), vol. 352, 122134
DOI: 10.1016/j.engstruct.2026.122134
Statut: Postprint (Author's version)

predefined standards: fixed column length of 0.36 m and assigned densities of steel (7850 kg/m³), concrete (2400 kg/m³), Chinese fir (450 kg/m³), poplar (380 kg/m³), larch (590 kg/m³), and CFRP (1600 kg/m³).

Fig. 27. TRM-XGBoost program interface.

Fig. 28. Single-instance prediction.

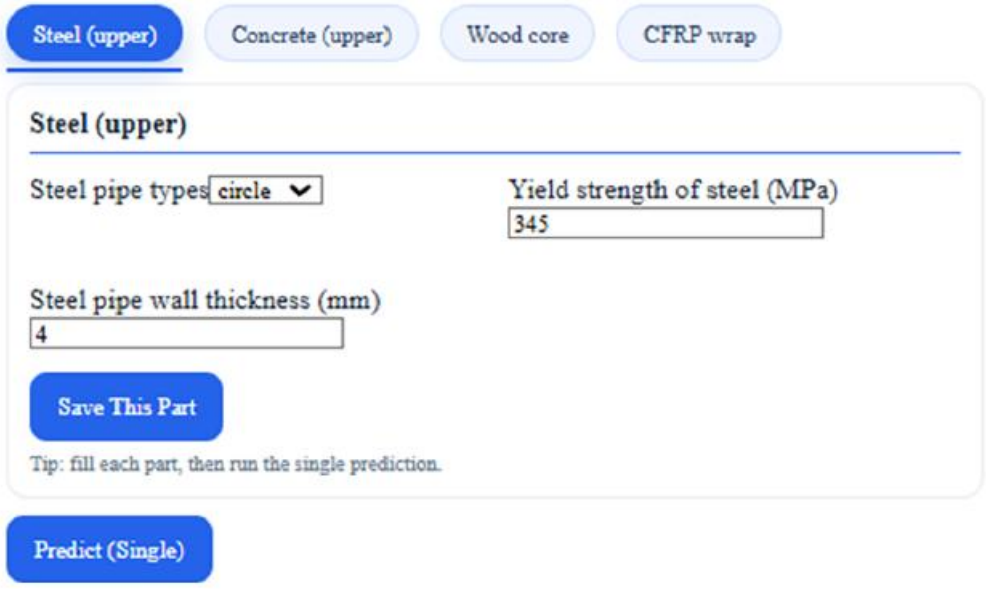

Published in: Engineering Structures (2026), vol. 352, 122134
DOI: 10.1016/j.engstruct.2026.122134
Statut: Postprint (Author's version)

The right panel functions as the results and interpretation zone (Fig. 29). For batch predictions, scrollable tables display predicted axial bearing capacities, corresponding self-weights, and an additional Capacity-to-Self-weight ratio column, thereby facilitating rapid comparison of lightweight performance across alternative design configurations. Beneath the tables, SHAP-based feature-importance bar charts provide interpretable analysis of TRM-XGBoost outputs by quantifying the average contributions of each input variable to the predictions while simultaneously preserving transparency and explainability.

Fig. 29. Batch predictions.

(a) Batch results column (b) Optimal combination column (c) SHAP display

As shown in Fig. 30, the diagram visualizes linear relationships between three key features, namely the predicted axial capacity (kN), self-weight (kg/m), and capacity-to-self-weight ratio. These relationships are derived from stepwise adjustments across 20 data groups, while all other features are held constant and excluded from the analysis. When the timber core size increases, the self-weight decreases significantly due to the substantially lower density of wood compared to concrete, although the predicted capacity experiences only a minor increase. Consequently, the capacity-to-self-weight ratio rises rapidly, enhancing overall structural efficiency. By contrast, increasing the steel tube wall thickness directly adds steel mass, causing both self-weight and predicted capacity to increase. However, because the relative rates of weight growth and capacity improvement differ, the capacity-to-self-weight ratio exhibits multiple inflection points, thereby providing users with a feedback mechanism to determine optimal design values. Regarding the enhancement of steel yield strength, it significantly improves predicted capacity without affecting self-weight, leading to a steady increase in the capacity-to-self-weight ratio. This confirms that increasing material strength can significantly enhance structural performance under constant weight conditions.

Fig. 30. Capacity to self-weight ratio analysis.

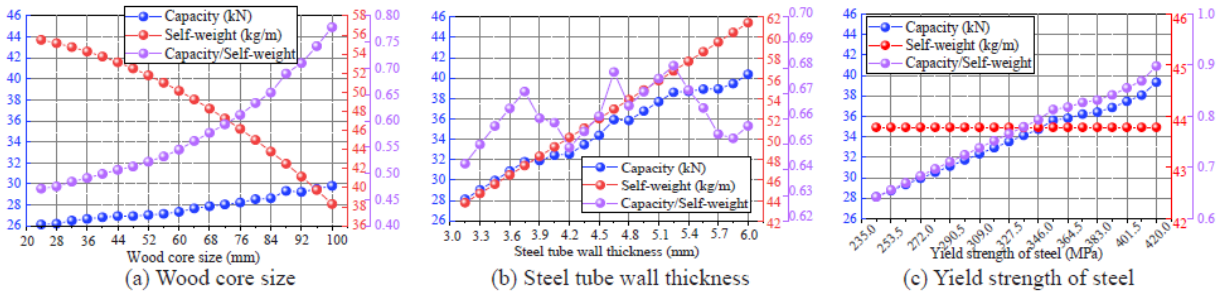

(a) Wood core size (b) Steel tube wall thickness (c) Yield strength of steel

Published in: Engineering Structures (2026), vol. 352, 122134
DOI: 10.1016/j.engstruct.2026.122134
Statut: Postprint (Author's version)

5.5. ENGINEERING IMPLICATIONS FOR PRACTICE

As shown in Fig. 31, the findings of this study have direct implications for structural engineering practice. Firstly, the demonstrated capacity gains from increasing steel yield strength and wall thickness clarify how material selection can be optimized under cost and weight constraints. For example, while a 6 mm wall thickness increases capacity by 64%, the associated weight growth requires balancing efficiency using the proposed capacity-to-self-weight ratio. Secondly, CFRP confinement not only improves ductility but also enables the use of lightweight timber cores, reducing structural self-weight by up to 22% without significant loss of capacity. This supports sustainable design by lowering material consumption while maintaining safety. Thirdly, the TRM-XGBoost prediction tool provides a rapid decision-support system that allows engineers to evaluate multiple design alternatives in real time, ensuring that composite columns can be tailored to diverse performance requirements. Collectively, these implications enhance Constructability, Cost-effectiveness, and Computer-aided (3C design procedure) in next-generation building systems [48].

Fig. 31. 3C design procedure.

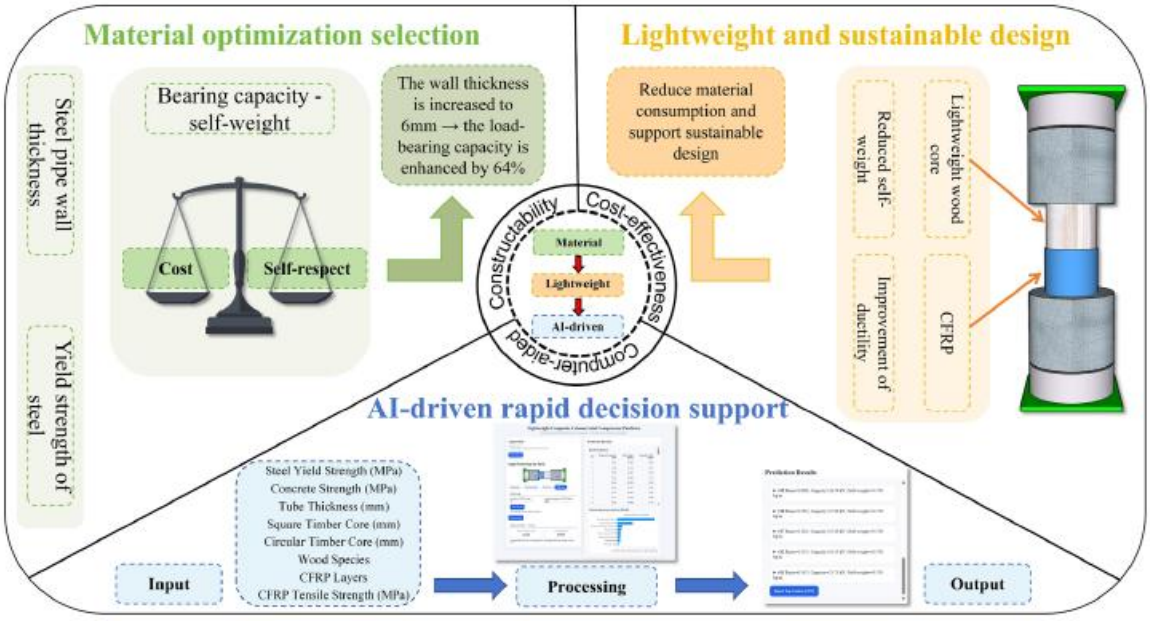

6. Conclusions

This study systematically investigated the axial compressive behavior of concrete-filled steel tubular columns with built-in CFRP-confined timber cores through theoretical model, finite element simulation, and machine learning approaches. The bearing capacity of this composite system is enhanced via multi-material synergy, where CFRP confinement effect, steel tube cross-sectional shapes, and timber core types exhibit decisive influences on mechanical performance. Key findings are summarized as follows:

(1) Increasing steel yield strength and tube thickness would enhance the capacity of the composite columns, whereas CFRP confinement improves the post-crushing response and

Published in: Engineering Structures (2026), vol. 352, 122134
DOI: 10.1016/j.engstruct.2026.122134
Statut: Postprint (Author's version)

ductility of the timber core. Parametric analysis confirm a 64% bearing capacity gain when steel tube wall thickness is increased to 6 mm, verifying the critical role of sectional stiffness in confinement effectiveness.

(2) The columns with circular cores exhibit better deformability than those with square ones. Circular tube configurations show CFRP confinement increases the timber core residual capacity by 15–20%, whilst circular timber cores exhibit 10–15% greater deformation ductility than square cores. Larch timber cores deliver 18% higher bearing capacity than Chinese fir, with timber-steel shape interactions granting square timber cores in square tubes a 15% capacity advantage.

(3) Theoretical derivations established the bearing capacity formulas incorporating multi-material confinement, introducing an equivalent confinement reduction coefficient. Unified strength theory resolves steel tube lateral confinement stresses, while a timber enhancement factor model is developed. The predictions by using the proposed theoretical formulas show less than 10% deviation from finite element data.

(4) Machine learning predicts the axial performance of lightweight composite columns using data from finite element simulations. The novel TRM-XGBoost model, integrating theoretical mechanics and residual correction, achieves a breakthrough accuracy of R^2 = 0.9873. A dedicated tool supports both single and batch predictions with parameter input and SHAP visualization, automatically computes self-weight, and outputs bearing capacity and weight metrics, enabling rapid optimization and supporting lightweight design decisions.

While the proposed framework has been validated through extensive finite element (FE) analyses and comparative evaluations, this study remains primarily simulation-oriented. The FE model, although carefully calibrated, inevitably adopts standard modeling idealizations, and further experimental evidence would be beneficial to strengthen the generality of the observed component-level mechanisms. In addition, the machine-learning dataset is generated from parametric FE cases, which provides consistent and controllable samples, but future work can further improve robustness by incorporating more experimentally measured data and broader practical variations. Moreover, the current work focuses on axial compression; extending the framework to other loading scenarios and longer-term performance considerations would enhance engineering applicability. These aspects will be pursued in future studies to further support reliable implementation in design practice.

CRediT authorship contribution statement

Jie Yang: Methodology, Investigation. **Jean Francois Demonceau:** Supervision, Conceptualization. **Feng Fu:** Conceptualization. **Zhenhua Huang:** Methodology, Conceptualization. **Shan Gao:** Writing – review & editing, Supervision, Conceptualization. **Jicheng Xu:** Writing – original draft, Visualization, Validation, Investigation.

Published in: Engineering Structures (2026), vol. 352, 122134
DOI: 10.1016/j.engstruct.2026.122134
Statut: Postprint (Author's version)

Data Availability Statement

The program developed in section 5.4 could be obtained in the Supplementary materials. Further inquiries can be directed to the corresponding author(s).

Declaration of Competing Interest

The authors declare that they have no known competing financial interests or personal relationships that could have appeared to influence the work reported in this paper.

Acknowledgements

This research was supported by the National Natural Science Foundation of China (Nos. 52278165, 51908085), Natural Science Basic Research Program of Shaanxi Province (No. 2024JC-YBMS-439), Scientific Research Program for Youth Innovation Team of Shaanxi Provincial Department of Education (No. 24JP201).

Appendix A. Supplementary material

Supplementary data associated with this article can be found in the online version at doi:10.1016/j.engstruct.2026.122134.

Data availability

Data will be made available on request.

References

[1] Wang YH, et al. Combined compression-bending-torsion behaviour of CFST columns confined by CFRP for marine structures. Compos Struct 2020;242:112181.

[2] Zhou Q. Theoretical study on axial compression behavior of timber columns strengthened with CFRP. Low Temp Archit Technol 2009;31(9):51–3 [+102].

[3] Wang Y, et al. Monotonic axial compressive behaviour and confinement mechanism of square CFRP-steel tube confined concrete. Eng Struct 2020;217: 110802.

Published in: Engineering Structures (2026), vol. 352, 122134
DOI: 10.1016/j.engstruct.2026.122134
Statut: Postprint (Author's version)

[4] Liu JP, Xu TX, Wang YH, et al. Axial behaviour of circular steel tube concrete stub columns confined by CFRP materials. Constr Build Mater 2018;171:650–65.

[5] Shao JS, Liu WQ, Wang GM, et al. Experimental study on axial compression behavior of FRP hoop-strengthened timber columns. Fiber Reinf Plast/Compos 2012;(2):4.

[6] Bukauskas A, Bock M, Harris R, et al. Whole timber construction: a state of the art review. Constr Build Mater 2019;213:748–69.

[7] Gao S. Life cycle sustainability assessment of concrete-filled steel tubular frames in earthquake regions. Eng Struct 2025;328:119761.

[8] Gao S, Yang J, Kang SB, et al. Experimental and numerical studies on deformation performance of square concrete-filled steel tubular columns under repeated lateral impacts. Eng Struct 2024;308:117909.

[9] Zhou CD, Liang LC, Asiha, et al. Experimental study on axial compression behavior of rectangular timber columns strengthened with embedded steel bars and externally wrapped CFRP sheets. J Build Struct 2020;41(7):9.

[10] Huang JJ, She YH, Zhang HF, et al. Experimental study on axial compression damage performance of CFRP-strengthened timber columns. Acta Mater Compos Sin 2024;41(9):5085–99.

[11] Jin S, Wei L, Tong J, et al. Stress-strain model for FRP-strengthened wood column under axial compression. Eng Mech 2008.

[12] Zhu YM, Long T, Hou M, et al. FRP reinforced short wood columns under axial compressive load. Adv Mater Res 2013;671-674(1):484–7.

[13] Liu P, Qian Z, Wang HR, et al. Experimental study on axial compression behavior of steel-wood composite columns. Eng Mech 2021;38(S1):8.

[14] Li GC, Xia XB, Qiu ZM, et al. Finite element analysis of axial compression performance of square steel tube-wood-concrete medium-long columns. J Shenyang Jianzhu Univ (Nat Sci) 2022;38(6):961–9.

[15] Wei B, Li H, Wang Y, et al. Compressive performance of bamboo scrimber and concrete-filled steel tube columns. Eng Struct 2024;300:117192.

[16] Yuan F, Chen J, Wang Y, et al. Effect of stiffeners on the eccentric compression behaviour of square concrete-filled steel tubular columns. Thin-Walled Struct 2019;142:1878–94.

[17] Xia X. Mechanical behavior of square steel tube-wood-concrete intermediate columns under axial compression. Shenyang Jianzhu Univ 2022.

[18] Li WJ, Liang HJ, Li S, et al. Analytical solution for predicting the interaction stress of axially loaded concrete-filled double-tube columns. Thin-Walled Struct 2022; 179:109579.

[19] Li W, Sun J, Wang K, et al. Refinement of unified design formula for CFST stub columns under axial compression. J Constr Steel Res 2025;226:109302.

[20] Vu Q, Truong V, Thai D, et al. Machine learning-based prediction of CFST columns using gradient tree boosting algorithm. Compos Struct 2020;259:113505.

Published in: Engineering Structures (2026), vol. 352, 122134
DOI: 10.1016/j.engstruct.2026.122134
Statut: Postprint (Author's version)

[21] Kang M, Yoo D, Gupta R. Machine learning-based prediction for compressive and flexural strengths of steel fiber-reinforced concrete. Constr Build Mater 2021;266: 121117.

[22] Chen MC, Li Q. Elastic mechanics analysis of composite elastic modulus and axial force distribution for concrete-filled steel tubular columns. J East China Jiaotong Univ 2016;33(4):24–30.

[23] Megahed K, Mahmoud NS, Abd-Rabou SEM. Finite element modeling for concrete- filled steel tube stub columns under axial compression. Int J Steel Struct 2024;24 (5).

[24] Mohammed M, Hasan MF, Hasan HF, et al. Axial compression tests for circular concrete-filled steel tube (CFST) columns with notch imperfection. KSCE J Civ Eng 2024;28(6).

[25] Ji J, Zhang W, Li G, et al. Nonlinear buckling analysis of H-type honeycombed composite column with rectangular concrete-filled steel tube flanges. Int J Steel Struct 2018;18(4):1153–66.

[26] Ren FM, Yang Y, Li Y, et al. Behaviour of FRP tube-concrete-encased steel composite columns. Compos Struct 2020;241:112139.

[27] Zhang Y, Wang JX, Fu F, Gao S, Niu XY. Mechanism and control method of anti- collapse resistance of novel bolted endplate joints. J Constr Steel Res 2026;237: 110142.

[28] Tao Z, Wang ZB, Yu Q. Finite element modelling of concrete-filled steel stub columns under axial compression. J Constr Steel Res 2013;89:121–31.

[29] Gao S, Xu YC, Zhang SM, Derlatka A. Performance of square concrete-filled steel tubular columns under repeated lateral impact. Eng Struct 2023;280:115719.

[30] Papanikolaou V, Kappos A. Confinement-sensitive plasticity constitutive model for concrete in triaxial compression. Int J Solids Struct 2007;44(21):7021–48.

[31] Uenaka K. Experimental study on concrete filled elliptical/oval steel tubular stub columns under compression. Thin-Walled Struct 2014;78:131–7.

[32] Yu T, Teng J, Wong Y, Dong S. Finite element modeling of confined concrete-I: Drucker-Prager type plasticity model. Eng Struct 2010;32(3):665–79.

[33] Gao S, Zhou LQ, Guo LH, et al. Temperature effect on mechanical performance of recycled glulam towards to sustainable production. J Clean Prod 2022;359: 132077.

[34] Song XB, Lam F. Stability capacity and lateral bracing requirements of wood beam- columns. J Struct Eng 2010;136(2):211–8.

[35] Tao JL, Yu ZS, Jiang P. Study on constitutive relationship of wood under static large deformation. Mech Eng 2000;22(5):25–7.

[36] Yue XH. Mechanical behavior of steel tube-wood-concrete stub columns under axial compression. Shenyang Jianzhu Univ 2020.

[37] Zhu YX. Experimental study on axial compression behavior of concrete-filled steel tubular stub columns with wood core. Suzhou Univ Sci Technol 2023.

[38] Zhao M. Research on axial compression behavior of FRP-confined GLT and CLT stub columns. Nanjing Forestry University; 2022.

Published in: Engineering Structures (2026), vol. 352, 122134
DOI: 10.1016/j.engstruct.2026.122134
Statut: Postprint (Author's version)

[39] Zhao JH, Zhang YQ, Li JC, et al. Unified limit solution of thick-walled cylinder for materials with different tensile and compressive strengths. Mech Eng 1999;21(6): 3–7.

[40] Li XW, Zhao JH, Zhu TD, et al. Mechanical properties of square concrete-filled steel tubular stub columns under axial compression. China J Highw Transp 2006;19(4): 77–81.

[41] Lam L, Teng J. Design-oriented stress-strain model for FRP-confined concrete in rectangular columns. Constr Build Mater 2009;17(6):471–89.

[42] Richard R, Abbott B. Versatile elastic-plastic stress-strain formula. J Eng Mech Div 1975;101(4):511–5.

[43] Toutanji H. Stress-strain characteristics of concrete columns externally confined with advanced fiber composite sheets. ACI Mater J 1999;96(3):397–404.

[44] Chun Q, Pan J. Experimental study on axial compression behavior of wood columns strengthened with carbon-aramid hybrid fiber sheets. J Build Mater 2011; 14(3):427–31.

[45] Gao S, Yang J, Chen XZ, Gao BY, Huang ZH. Axial compression behavior of steel tubular members with simulated splashing corrosion. Structures 2025;80:109873.

[46] Gao S, Zeng QK, Wang JX, Huang ZH, Zhang Y. Mechanistic–data-driven modeling of tensile strength reduction in locally damaged square steel tubes. Structures 2025;80:110072.

[47] Liu KZ, Wang JF, Gao S, Xu M. Mechanical–data-driven performance interpretation and design of concrete-filled steel tubes under lateral impact. J Constr Steel Res 2026;238:110204.

[48] Zhang T, Zhu RX, Gao S. Compressive behavior of coal gangue concrete-filled steel tube in cold region towards to sustainability design. Constr Build Mater 2026;506: 145002.